

# Gut Flora-Targeted Photobiomodulation Therapy Improves Senile Dementia in an A $\beta$ -Induced Alzheimer's Disease Animal Model

**Qianqian Chen**

Chinese Academy of Medical Sciences & Peking Union Medical College Institute of Biomedical Engineering

**Jinpeng Wu**

Chinese Academy of Medical Sciences & Peking Union Medical College Institute of Biomedical Engineering

**Huijuan Yin** (✉ [yinhj@bme.pumc.edu.cn](mailto:yinhj@bme.pumc.edu.cn))

Chinese Academy of Medical Sciences & Peking Union Medical College Institute of Biomedical Engineering <https://orcid.org/0000-0002-4821-7562>

**Xiaoxi Dong**

Chinese Academy of Medical Sciences & Peking Union Medical College Institute of Biomedical Engineering

**Xiafei Shi**

Chinese Academy of Medical Sciences & Peking Union Medical College Institute of Biomedical Engineering

**Siying Su**

Chinese Academy of Medical Sciences & Peking Union Medical College Institute of Biomedical Engineering

**Boshen Che**

Chinese Academy of Medical Sciences & Peking Union Medical College Institute of Biomedical Engineering

**Yingxin Li**

Chinese Academy of Medical Sciences & Peking Union Medical College Institute of Biomedical Engineering

---

## Research

**Keywords:** Alzheimer's Disease, Photobiomodulation Therapy, Gastrointestinal Microbiome, Proteomics

**Posted Date:** November 13th, 2020

**DOI:** <https://doi.org/10.21203/rs.3.rs-104542/v1>

**License:** © ⓘ This work is licensed under a Creative Commons Attribution 4.0 International License.

[Read Full License](#)

---

**Version of Record:** A version of this preprint was published at Journal of Photochemistry and Photobiology B: Biology on March 1st, 2021. See the published version at <https://doi.org/10.1016/j.jphotobiol.2021.112152>.

# Abstract

**Background:** Emerging evidence suggests that the gut microbiota plays an important role in the pathological progression of Alzheimer's disease (AD). Photobiomodulation (PBM) therapy is believed to have a positive regulatory effect on the imbalance of certain body functions, including inflammation, immunity, wound healing, nerve repair, and pain. Previous studies have found that the intestinal flora of patients with AD is in an unbalanced state. Therefore, we have proposed the use of gut flora-targeted PBM (gf-targeted PBM) as a method to improve AD in an A $\beta$ -induced AD mouse model.

**Methods:** PBM was performed on the abdomen of the mice at the wavelengths of 630 nm, 730 nm, and 850 nm at 100 J/cm<sup>2</sup> for 8 weeks. Morris water maze test, immunofluorescence and proteomic of hippocampus, and intestinal flora detection of fecal were used to evaluate the treatment effects of gf-targeted PBM on AD rats.

**Results:** PBM at all three wavelengths (especially 630 nm and 730 nm) significantly improved learning retention as measured by the Morris water maze. In addition, we found reduced amyloidosis and tau phosphorylation in the hippocampus by immunofluorescence in AD mice. By using a quantitative proteomic analysis of the hippocampus, we found that gf-targeted PBM significantly altered the expression levels of 509 proteins (the same differentially expressed proteins in all three wavelengths of PBM), which involved the pathways of hormone synthesis, phagocytosis, and metabolism. The 16s rRNA gene sequencing of fecal contents showed that PBM significantly altered the diversity and abundance of intestinal flora. Specifically, PBM treatment reversed the typical increase of *Helicobacter* and uncultured *Bacteroidales* and the decrease of *Rikenella* seen in AD mice.

**Conclusions:** Our data indicate that gf-targeted PBM regulates the diversity of intestinal flora, which may improve damage caused by AD. Gf-targeted PBM has the potential to be a noninvasive microflora regulation method for AD patients.

## 1. Introduction

Alzheimer's disease (AD) is a typical degenerative disease of the central nervous system. It is characterized by cognitive impairment, progressive memory loss, behavioral and social impairment, and dementia (1). The 2018 World Alzheimer's Report states that AD is both a human problem and a global problem. Every 3 seconds, there will be a new case of dementia in the world. About 50 million people worldwide had AD in 2018, and that number is expected to rise to 152 million by 2050 (2). The main pathological feature of AD is senile plaques, which result from amyloid  $\beta$  protein (A $\beta$ ) aggregation in the brain. These plaques are tangles formed by tau protein hyperphosphorylation. Plaque formation leads to the dysfunction of neurons and synapses and chronic, long-term inflammation in the brain, which ultimately results in neural degeneration (3). Although the pathogenesis of AD is still unknown, four hypotheses have been put forward in view of these major neuropathologic features, namely the amyloid- $\beta$  hypothesis, the tau protein hypothesis, the neurotransmitter disorder hypothesis, and the chronic

inflammation hypothesis (4). Based on these hypotheses, several drugs based on different pathological mechanisms have been developed (5). Currently, there are five AD drugs approved by the US Food and Drug Administration, including donepezil, rivastigmine, galantamine, huperzine, and memantine (6). However, these drugs mainly improve symptoms, and there is no drug that will delay disease progression or cure AD.

Recent studies have shown that the intestinal flora is involved in the occurrence and development of AD through a variety of pathways. Therefore, intestinal flora modulation is now being considered as a new target for the treatment of AD (7, 8). The intestinal flora mainly affects the occurrence of AD through the nervous system, the endocrine system, metabolism, and immunity (9, 10). In some animal and human studies, researchers have attempted to regulate the intestinal flora to prevent and treat AD. For example, Woo et al. found that administration of sugar-free *Lactobacillus* plant varieties C29 by gastric perfusion to a cognitively-damaged mice model significantly improved memory dysfunction caused by D-galactose and increased the expression of BDNF (Brain Derived Neurotrophic Factor) in the brain. This reduced the expression of aging marker P16, inflammatory markers p-p65 and p-foxa3a, cyclooxygenase-2, and inducible nitric oxide synthase, and inhibited the expression of TNF- $\alpha$  induced by D-galactose (11). A randomized, double-blind, controlled clinical trial of patients with AD also confirmed that there was a significant difference in the degree of improvement in cognitive and metabolic functions in patients who received mixed probiotics (*Lactobacillus acidophilus*, *Lactobacillus casei*, *Bifidobacterium bifidum*, and *Lactobacillus fermentum*) in their milk compared with patients in the sterilized milk intake group (12).

Photobiomodulation (PBM) therapy, also called low-level laser therapy, is a noninvasive light therapy that uses a low power non-thermal light source to irradiate target tissues and regulate body functions. PBM has been effectively applied in many clinical diseases, including chronic shoulder and neck pain, wound healing, jaw joint disorders, oral mucositis, arthritis, muscle injury, bone regeneration, diabetic foot disease, multiple sclerosis, Parkinson's disease, and AD (13, 14). The wavelength of red and infrared irradiation is most commonly used because it penetrates deep into tissue, affecting metabolic modifications, DNA activity, ATP formation, and the mitochondrial chain. The effect of PBM is due to the absorption of photons by cytochrome C oxidase in the mitochondrial respiratory chain, which consequently increases cytochrome C oxidase activity and therefore ATP formation. ATP from injured regions or regions of impaired blood perfusion can reactivate injured cells and help treat metabolic disorders (15–17). PBM is also related to pain relief, inflammation relief, and the prevention of tissue death to avoid neurological degeneration (18, 19). PBM is considered a method of adjusting the imbalance of body functions within a certain range and eventually establishing a new balance. The intestinal flora of patients with AD is in an unbalanced state, with a decrease in beneficial flora and an increase in harmful flora, which leads to the consequential imbalance of inflammation and immunity and eventually induces or aggravates AD. PBM may be useful for regulating the imbalance of intestinal flora in AD.

PBM has a bidirectional regulatory effect on bacteria. This therapy can promote bacterial proliferation or inhibit bacterial growth, depending on the wavelength and dose of PBM and the type of bacteria (20).

Under blue and green light (400–500 nm), bacterial growth was inhibited or inactivated by irradiation with 10–200 J/cm<sup>2</sup> light. For example, 95% of *Pseudomonas aeruginosa* could be inactivated by a 405 nm laser at 10J/cm<sup>2</sup>, and 90% of *Staphylococcus aureus* could be inactivated by 15 J/cm<sup>2</sup> (21). However, under the irradiation of red and infrared light, the proliferation of bacteria was accelerated at low (1–10 J/cm<sup>2</sup>) light intensities. Interestingly, 810 nm laser irradiation of 5 J/cm<sup>2</sup> could accelerate the proliferation of *Escherichia coli*, while 23% of *Pseudomonas aeruginosa* was inhibited under the same conditions (22). The bidirectional regulation of PBM on bacteria makes it possible to improve the imbalance of the gut flora in AD patients. In this study, we proposed the method of gut flora-targeted photobiomodulation therapy (gf-targeted PBM) and explored its improvement of AD in an A $\beta$ -induced AD mouse model.

## 2. Materials And Methods

### 2.1 Animals

Male C57BL/6N mice with an average body weight of 24–28 g were used in this study. Mice were obtained from Beijing Vital River Laboratory Animal Technologies Co. Ltd. Mice were fed in cages of 7–8 animals, with free drinking water and food.

The mice were anesthetized by an intraperitoneal injection of 0.1 mL 5% chloral hydrate. The mice were fixed on a stereotactic brain apparatus, the head skin was shaved, disinfected, cut along the midline, and the fascia was removed. The skull surface was wiped with hydrogen peroxide, exposing the bregma (anterior fontanelle) point. The bilateral hippocampal CA1 area, 2.3 mm behind the anterior fontanelle and 1.8 mm beside the sagittal seam, was used as the drug administration point. The injection depth was 2.0 mm below the skull surface. Then, 1.0  $\mu$ L A $\beta$ <sub>1–42</sub> of 3M was injected bilaterally into the hippocampus over a period of 0.2  $\mu$ L/min using a 1  $\mu$ L microsyringe. The needle was left in for 5 min to allow for complete diffusion of the drug, followed by suturing the skin.

### 2.2 Gf-targeted PBM treatment

The mice were randomly assigned into four groups: PBM630 (irradiation with 630 nm LED), PBM730 (irradiation with 730 nm LED), PBM850 (irradiation with 850 nm LED), and Ctrl M (control model mice, untreated with PBM). There were 15 mice in each group. Another 15 C57BL/6N mice without A $\beta$ <sub>1–42</sub> induction were set as the group of Ctrl B (control blank mice).

The PBM process was carried out as follows. After isoflurane anesthesia, the mice were fixed in the supine position to fully expose the abdomen and remove the abdominal hair. The special LED irradiation device for the laboratory (with wavelengths of 630 nm, 730 nm, and 850 nm) was fixed on the upper abdomen of the mice, with the LED irradiation surface facing the abdomen. The PBM device was operated in the dark. The irradiation time was 1000s (16 min and 40 s), the power density was

10 mW/cm<sup>2</sup>, and the energy density was 100 J/cm<sup>2</sup>. The treatment occurred once a day, 5 times a week, for 8 weeks.

## **2.3 Morris water maze test**

A Morris water maze (MWM) test was performed to evaluate the improvement of learning ability (navigation test) and memory ability (spatial probe test) of mice before and after PBM interventions. The MWM test was divided into a training period (3 days), a positioning cruise period (6 days), and a space exploration period (1 day). During the training period, the platform was located in the same position (one of four quadrants of the pool), and the mouse was placed into the pool facing the platform. The mouse was removed from the water when it located the platform. If the mouse did not find the platform after 120 s of swimming, it was gently guided to the platform or placed on the platform for 15 s before being removed from the pool. For the navigation test, the movement of the mouse was tracked by a digital tracking system. The latency, the percent time in the outer annulus, the average swimming speed, the swimming trajectory, and the search strategy were recorded to evaluate the spatial learning ability of the animals. The mice were tested twice per day. For the spatial probe test, the platform was removed from the pool and the mouse was placed in the pool in a random quadrant. The movement tracking was recorded for 2 min.

## **2.4 Sample preparation**

After the last MWM test, the mice were sacrificed in a state of deep anesthesia (10% chloral hydrate injected intraperitoneally) for the collection of the brain tissues, mesenteric lymph nodes, blood samples, and fresh fecal samples. Blood samples were obtained by eyeball extraction. Stool samples were collected by squeezing a section of the colon removed from the mice. Cardiac perfusion was performed with normal saline before brain tissue was taken. Bilateral hippocampal tissues were removed within 10 min for frozen section preparation and proteomics detection, as were mesenteric lymph nodes for pathological section preparation.

## **2.5 Mesenteric blood flow observation by laser speckle**

On the day after the end of PBM treatment, 3 mice were taken from each group and anesthetized. Then, the abdominal skin of each animal was cut open to expose the mesentery and small intestine, which were placed 28–30 cm under the lens. Blood flow pattern images were collected by laser speckle (Moor FLPI, Wilmington, DE, USA). The average blood perfusion value was automatically generated by the moorFLPI system software and the vessel diameter was calculated by ImageJ software.

## **2.6 Immune response detected by ELISA and immunohistochemistry**

Serum was isolated from blood samples and used to detect inflammatory factors IL-6 (RAB0308, Sigma) and INF- $\gamma$  (RAB0224, Sigma) using ELISA kits. Mesenteric lymph nodes were fixed with 4% paraformaldehyde (0.01 M, pH 7.4, 4°C) for 24–48 hours, and were routinely dehydrated, transparent, waxed, and embedded. Sections with a thickness of 5  $\mu$ m were sliced on the paraffin sectioning machine

and placed on the slides treated with poly acid for baking at 60°C for 4–6 hours and stored. Immunohistochemistry for CD45 and CD11b antigens was performed. Antigens were unmasked by microwaving sections in 10 mmol/L citrate buffer, pH 6.0 (15 min), and immunostaining was undertaken using the avidinbiotinylated enzyme complex method with antibodies against CD45 (ab10558, Abcam) at a concentration of 1 µg/ml, CD11b (ab133357, Abcam) at a concentration of 1 µg/ml, and biotin-conjugated secondary antibody at a concentration of 1 µg/ml.

## 2.7 Immunofluorescence staining

For frozen section preparation, hippocampus tissue was dehydrated in gradient sucrose solutions (with concentrations of 10%, 20%, and 30%) for 24 h, with the brain tissue sinking to the bottom of the tube. Then, the tissue was embedded by optimum cutting temperature compound and quick-frozen for 10 min in a low-temperature freezing slicing machine. Slices of 50 µm thickness were cut along the coronal plane. Immunofluorescence staining was performed to observe the expression of A $\beta$ <sub>1–42</sub>, Iba1, and phosphorylated tau protein. Rabbit-anti-beta Amyloid 1–42 (ab224025, Abcam), Rabbit-anti-Iba1 (ab225260, Abcam), Rabbit-anti-Tau (phospho S396) (ab109390, Abcam), and the secondary antibodies Alexa Fluor® 488 AffiniPure Goat Anti-Rabbit IgG (H + L) (111-545-003, Jackson ImmunoResearch, West Grove, PA, USA) for Iba1 and Tau and Rhodamine (TRITC) AffiniPure Goat Anti-Rabbit IgG (H + L) (111-025-003, Jackson ImmunoResearch, West Grove, PA, USA) for A $\beta$ <sub>1–42</sub> were used in immunofluorescence staining. Immunofluorescence images were obtained using an automatic scanning system (C13210-01; Hamamatsu Photonics, Hamamatsu City, Japan).

## 2.8 Proteomic detection and data analysis

Proteins extracted from fresh hippocampus tissues (stored at – 80°C) were pooled from 5 mice of each group for LC-MS/MS analysis combined with tandem mass tags (TMT) labeling. Briefly, the pooled protein samples from five groups of PMB630, PBVM730, PBM850, Ctrl B, and Ctrl M were cleaved into peptides with 1 µg/µL trypsin and isobaric labeled TMT. Equal protein amounts derived from each group were labeled with different TMT labels: Ctrl B, TMT-126; Ctrl M, TMT-127N; PMB630, TMT-128N; PMB730, TMT-128C; and PMB850, TMT-129N. The labeled peptides were mixed, dried, and then fractionated into 16 fractions by HPLC. Following fractionation, each peptide fraction was desalted and purified by C18 reverse phase chromatography. Then, the mass spectrometry data were analyzed using Q-Exactive MS (Thermo Fisher Scientific, Waltham, MA, USA). The parameters for LC-MS/MS are shown in Table 1.

Table 1  
The parameters for LC-MS/MS.

	Item	Parameter
NanoLC	NanoLC trap	Acclaim PePmap 100 150 $\mu\text{m}$ $\times$ 2 cm nanoviper C18 5 $\mu\text{m}$ 100 $\text{\AA}$
	Solvent A	0.1% formic acid 2% ACN 98% water
	Solvent B	0.1% formic acid 2% water 98% ACN
	Flow rate	0.4 $\mu\text{l}/\text{min}$
	NanoLC column	C18 5 $\mu\text{m}$ 75 $\mu\text{m}$ $\times$ 15 cm 300 $\text{\AA}$
Q-E MS	Polarity	positive ion mode
	MS scan range	350–2000 m/z
	Resolution	35000
	Capillary temperature	320 $^{\circ}\text{C}$
	Ion source voltage	1800V
	MS/MS acquisition modes	Higher collision energy dissociation(HCD)
	Normalized collision energy (NCE)	30

A false discovery rate less than 1.0% was selected for peptides only. Precise quantification of protein was expressed as the protein ratio between samples, and differentially expressed proteins (DEPs) were selected at  $p < 0.05$  by a Student's  $t$  test. The thresholds of up- and downregulated ratios were set at 1.2 and 0.83, respectively. The proteomic data distribution patterns, volcano plots, and heatmap were created using Thermo Fisher Proteome Discoverer 1.4. The DEPs of the PBM group were determined compared with the Ctrl M group and the cluster analysis of DEPs was performed using the gene ontology (GO) and KEGG pathway database.

## 2.9 Fecal DNA extraction and 16 s rRNA gene sequencing

A DNA extraction kit (DNeasy PowerSoil Kit; Qubit dsDNA Assay Kit, Qiagen, Germany) was used to extract the genomic DNA from the fecal samples ( $n = 5$ ). After that, the purity and concentration of DNA were detected by agarose gel electrophoresis. Appropriate samples were placed in a centrifuge tube and diluted to a concentration of 1 ng/ $\mu\text{L}$  in sterile water. The diluted genomic DNA was used as the PCR template. Specific primers with barcodes and a high-fidelity enzyme (Takara Ex Taq, Takara, Japan) were used for PCR according to the selected sequencing area to ensure amplification efficiency and accuracy. The V3–V4 hypervariable regions of the bacterial 16S rRNA gene were amplified with primers 343F (5'-TACGGRAGGCAGCAG-3') and 798R (5'-AGGGTATCTAATCCT-3') by a PCR system (Bio-Rad, Hercules, CA,

USA). PCR products were detected by electrophoresis and purified by magnetic beads. After purification, the PCR products were used as a two-round PCR template. Then, the DNA was detected and purified again, and quantified using a Qubit (Invitrogen Qubit 4 fluorometer, Thermo Fisher Scientific). Finally, the samples were mixed according to the concentration of PCR products and sequenced on the Illumina MiSeq platform (San Diego, CA, USA).

The original data were in FASTQ format. Trimmomatic software (Illumina) was used to remove clutter from the original double-ended sequence. When the base mass was less than 20, the previous high-quality sequence was intercepted. After the sequencing data were preprocessed to generate high-quality sequences, Vsearch software (<https://github.com/torognes/vsearch>) was used to classify the sequences into multiple OTUs according to the similarity of the sequences. Sequence similarities greater than or equal to 97% were classified as an OTU unit. The representative sequences of each OTU were selected using the QIIME software package (<http://qiime.sourceforge.net/>), and all the representative sequences were compared with the Silva (version 132) database for annotation. The RDP classifier software (23) was used for the species alignment annotation, leaving the annotation results with a confidence interval greater than 0.7.

## 2.10 Statistical analyses

All data with error bars are represented as mean  $\pm$  SEM. For two group comparisons, an unpaired two-tailed Student's *t* test was applied. For more than two group comparisons, a one-way ANOVA was performed.  $P < 0.05$  was considered statistically significant. The original ab2020 (OriginLab Corporation, Northampton, MA, USA) was used for data statistical analysis and figure production. For image quantification, ImageJ with IHC profiler (<https://imagej.net/>) was used.

## 3. Results

### 3.1 The scheme of gf-targeted PBM treatment for AD mice

The purpose of this study was to explore whether gf-targeted PBM can improve the symptoms and pathology of AD by regulating the intestinal flora. We produced the AD mouse model by A $\beta$ <sub>1-42</sub> injection and verified the modeling effect by a MWM test in ten mice. The AD mice then received the PBM intervention with different wavelengths for up to two months. After PBM treatment, the cognitive function of AD mice was determined by a MWM test and the changes in A $\beta$  amyloid protein, tau protein, microglia cells, and proteomics of hippocampal tissue were detected to determine the therapeutic effect of PBM on AD. In addition, we calculated the intestinal flora diversity after gf-targeted PBM to analyze both the regulatory effect of PBM on the intestinal flora and the abundance of beneficial flora following PBM-treated AD. Finally, we measured cellular immunity in the mesenteric lymph nodes and inflammatory factors in the blood to explore the role of immunity and inflammation as mediators in the treatment of AD by PBM. The design scheme of the complete experiment is shown in Fig. 1.

## 3.2 Gf-targeted PBM improves the cognition impairment of AD mice

The MWM experiment was divided into two parts: the location navigation test and the space probe test. The former tested the learning ability of AD mice and the latter tested the memory ability of AD mice.

Figure 2A shows that all three PBM groups improved the escape latency period (the time period from the mouse entering the water to finding the platform) in the 6-day navigation experiment. In the later period of the experiment, the performance of mice in the PBM group was better than that of the Ctrl M group, which was close to the normal mice in the Ctrl B group. For the percent of time in the outer annulus, PBM630, PBM730, and PBM850 all decreased the searching time of AD mice in the outer annulus of the pool compared with the untreated AD mice in the Ctrl M group. PBM630 showed the highest effect, as the PBM630-treated AD mice performed the same as the normal mice in the Ctrl B group on the second day. Interestingly, the swimming speed of mice in the three PBM groups was higher than that of the Ctrl M and Ctrl B groups, especially those in the PBM730 group. Untreated AD mice swam as fast as the normal mice in our study, which implies that the method of AD model building by A $\beta$ <sub>1-42</sub> injection did not impact the athletic ability of the mice. However, there was no significant difference between the three PBM groups in all the measurements, including latency, percent time in the outer annulus, and swimming speed.

We also analyzed the search strategies of the mice. The results are shown in Fig. 2B. Compared with Ctrl B, most of the mice in the Ctrl M group swam on the edge of the pool (dark grey bar) and searched randomly (blue bar), while trend type (red bar) of the mice in the PBM group took up a larger proportion when swimming in the later period of the experiment (after the 3rd day). This was especially evident in the mice from groups PBM630 and PBM850, as they could swim in a straight line towards the platform (green bar). The searching strategy scores of the three PBM groups (PBM630, PBM730, and PBM850) were significantly higher than those of the Ctrl M group ( $p = 0.004, 0.013, \text{ and } 0.001$ , respectively). Moreover, the scores of the PBM850 group recovered close to the Ctrl B group, indicating that the learning ability of AD mice after PBM850 treatment returned to a normal mouse level.

The memory ability of AD mice was measured in a space probe test. Figure 2C-F shows the swimming trajectory, times of traversing the platform, and the percent time in platform quadrants of the mice in the space probe test. The swimming trajectories of the normal mice were near the platform after they were put into the pool, while the AD mice in neither the Ctrl M group nor the PBM groups performed chaotic trajectories. By analyzing these trajectories, we found that regardless of the number of platform traversing times or the percentage of time in a platform quadrant, there was no significant difference between the three PBM groups and the Ctrl M group. This finding suggests that PBM had no effect on the memory ability of AD mice.

## 3.3 Improvement of pathology in brains of AD mice

Pathological changes in AD, such as A $\beta$  amyloid plaques, phosphorylated tau proteins (p-tau(s396)), and microglial cell activation are shown in Fig. 3. A $\beta$  amyloid plaques were clustered in the upper edge of the

hippocampus in Ctrl M mice. The PBM630 and PBM730 eliminated most of the clusters of A $\beta$  amyloid plaques which should be present in the hippocampus of mice. However, PBM850 with a long irradiation time only weakly affected A $\beta$  amyloid plaques (the upper right box in Fig. 3 showing the A $\beta$ <sub>1-42</sub> image of PBM850). In accordance with the results of A $\beta$  amyloid plaques, a mass of microglial cells (stained by Iba1) clustered in the hippocampus of Ctrl M and PBM850 mice, whereas only a few microglial cells were clustered in the PBM630 and PBM730 groups. A number of phosphorylated tau proteins were also present in the hippocampus of Ctrl M and PBM850 mice. Encouragingly, p-tau protein was virtually absent in the hippocampus of mice in the PBM630 and PBM730 groups. These results imply that irradiation with PBM630 and PBM730 contributes to the elimination of A $\beta$  amyloid plaques and inhibits the neuroinflammation and tau phosphorylation caused by A $\beta$  amyloid plaques.

### **3.4 Response of mesenteric blood flow and the immune system after PBM treatment**

We observed the mesenteric blood flow of mice using a laser speckle technique. The results are showed in Fig. 4A–C. We found that the blood flow of AD mice increased significantly compared with normal mice ( $p = 0.017$ ). However, the PBM intervention did not correct this abnormal increase. We also observed that PBM increased the blood vessel diameter, which seems to have little substantial effect on AD development.

Mesenteric lymph nodes are an important part of the body's immune system. To determine whether gf-PBM regulates AD by stimulating the intestinal mucosal immune system, we performed immunostaining for CD45 (marker for leukocytes) and CD11b (marker for phagocytes) in the mesenteric lymph nodes. As shown in Fig. 4F, we observed no significant difference between the groups when the positive cells were counted by ImageJ. In addition, we detected proinflammatory cytokines IL-6 and INF- $\gamma$  (Fig. 4D), which reflect humoral immunity. Both IL-6 and INF- $\gamma$  were inhibited in AD mice. PBM630 and PBM730 significantly increased the levels of INF- $\gamma$  in AD mice and exceeded the levels in normal mice (8.37-fold,  $P = 0.0004$ , and 3.97-fold,  $P = 0.018$ , respectively).

### **3.5 Proteomic changes in the hippocampus after gf-targeted PBM**

The original mass spectrometry data from the hippocampus of five groups of mice were filtered and searched by false discovery rate (FDR) < 1%. A total of 3,872 proteins were identified, matching 17,296 peptides and 289,377 spectra. A quantitative analysis was carried out on samples according to the peak strength of tagged ions, and the number of DEPs obtained ( $p < 0.05$ ) is shown in Fig. 5A and 5B. A fold-change of DEPs greater than 1.2 is upregulated (red) and a fold-change of less than 0.8 is downregulated (green). Compared with Ctrl M group, the number of DEPs in the hippocampal tissues of groups PBM630 and PBM730 were 1,209 and 1,329, respectively, while the number of DEPs in PBM850 was 634. We found that the DEPs between groups PBM630 and PBM730 groups was low, while the DEPs between

PBM850 and PBM630 or PBM730 was high. This indicates that the mechanisms of action associated with the PBM630 and PBM730 treatments may be similar, while the PBM850 treatment may occur via other mechanisms. The heat map in Fig. 5B shows that the expression of DEPs (compared with Ctrl M) in the PBM groups is opposite to Ctrl M. This indicates that PBM treatment corrects the abnormal changes in hippocampal proteins induced by AD.

The DEPs (compared with Ctrl M) of the three PBM groups were analyzed by GO classifications, including cellular components, molecular functions, and biological processes, to obtain functional annotation information from each protein. The first five proteins with the lowest p values are shown in Fig. 5C. In the PBM630 and PBM730 groups, DEPs were similar in terms of cellular components, molecular functions, and biological processes involved. For example, cellular components were mostly parts of proteins that composed cells and cytoplasm, molecular functions were mainly related to binding, and the biological processes involved were reorganization of cellular components and regulation of biological processes. Group PBM850 had both shared and unique DEPs compared with groups PBM630 and PBM730. For example, some DEPs in group PBM850 are components of neuronal projection. For molecular functions, some DEPs are related to G protein-coupled receptors, and for biological processes, the DEPs are more involved in the negative regulation of metabolic processes.

We also used the KEGG database to analyze the DEPs of the three PBM groups in Pathway. In all pathways with a p value of less than 0.05, the ratio of DEPs in background proteins of a pathway were sorted, as shown in Fig. 6. In the pathway of AD, the proportion of DEPs in the three PBM groups was high, with values of 58.7% (PBM630), 50.8% (PBM730), and 31.7% (PBM850). Mitochondrial respiratory chain complex enzymes were most affected by PBM (the lower right corner in Fig. 6) and Cx1 was downregulated, while Cx11 and Cx15 were upregulated under the three PBM treatments. CytC, a key member of the apoptosis pathway, was also downregulated in the PBM groups. In addition, Tau, RTN3/4, and SNCA, which all take part in AD development, were downregulated by the PBM interventions. Furthermore, some DEPs were involved in oxidative phosphorylation, phagocytosis, metabolism of some biological macromolecules, and most importantly, the secretion of many hormones, including insulin, thyroxine, and glucagon. The pathways associated with the DEPs of the PBM850 group were less than that of PBM630 and PBM730.

We also conducted a comparative analysis of the DEPs in the three PBM groups and found that there were 1,007 identical DEPs in PBM630 and PBM730, and 509 identical DEPs in PBM630, PBM730, and PBM850. We performed GO and KEGG pathway analyses on these 509 common DEPs to elucidate the possible association between the mechanism of AD treatment with gf-targeted PBM. The results are shown in Fig. 7. Many of the common DEPs are related to components in the cell and on the cell membrane, specifically, the binding of G protein complexes and receptors on the cell membrane and the binding of the cytoskeleton, RNA, and proteins. These DEPs are mainly involved in the negative regulation of cellular processes such as metabolism, especially the metabolism of nitrogen compounds, and the regulation of transport and localization. For the KEGG pathway analysis, in addition to the DEPs associated with AD, the DEPs are mainly involved in oxidative phosphorylation, calcium signaling

pathways, inflammation, phagocytosis, the secretion of various hormones (such as thyroid hormones, parathyroid hormones, aldosterone, renin, cortisol, and insulin), and the formation of synaptic structures. These findings imply that inflammation, repair, and reconstruction are all related to the improvement of AD with PBM.

### 3.6 Changes of intestinal flora diversity after gf-targeted PBM treatment

We compared the changes in intestinal flora diversity of each group after PBM treatment using 16S rRNA gene amplicon sequencing. Figure 8A shows the principal components analysis (PCA) of gut microbiome composition at the operational taxonomic unit (OTU) level for the mice. The gut flora of the five groups clustered separately, and the clusters of the three PBM groups were located between the clusters of the AD mice and the normal mice. ANOVA and Kruskal–Wallis tests were used to analyze the species with significant differences between groups. As shown in Fig. 8B, there were differences at all taxonomic levels, especially at the genus level. A boxplot analysis was conducted to determine the relative abundances of four of the top ten species present at different levels among the study groups. As shown as Fig. 8C, the abundances of *Helicobacter*, *Oscillibacter*, *Ruminiclostridium-5*, and uncultured *Bacteroidales* increased, while *Rikenella*, *Desulfovibrio*, *Ruminococcus-2*, and *Butyricicoccus* decreased in AD mice compared with the normal mice. PBM treatment corrected this imbalance of bacteria to some extent. In particular, all PBM treatments (PBM630, PBM730 and PBM850) reversed the increase of *Helicobacter* and uncultured *Bacteroidales* and the decrease of *Rikenella* in AD mice. Some of the findings were wavelength-specific. For example, PBM630 decreased the abundance of *Oscillibacter*, PBM730 increased the abundance of *Desulfovibrio* and *Ruminococcus-2*, and PBM850 corrected the imbalance of *Butyricicoccus* and *Ruminiclostridium-5* in AD mice. All PBMs decreased the abundance of *Ruminococcus-1*. However, the abundance of *Ruminococcus-1* was not significantly different between the AD and normal mice. We also performed a KEGG function prediction based on the 16S sequencing data, conducted a statistical analysis among groups according to the Kruskal–Wallis algorithm, and homogenized the results to form a heat map (Fig. 8D). We found that the functional composition of the intestinal flora in AD mice was different from that of normal mice, especially for pyrimidine metabolism, lipopolysaccharide synthesis, and bacterial toxins. PBM630 and PBM850 performed to correct the functional abnormality, bringing the functional composition closer to that of the normal flora.

## 4. Discussion

We applied PBM to the abdomen (referred to as gf-targeted PBM) rather than the brain of AD mice to verify whether PBM could interfere with the AD process by regulating gut flora. Encouragingly, we confirmed that the gf-targeted PBM treated AD by eliminating A $\beta$  plaques and inhibiting neuroinflammation and tau phosphorylation. The diversity and abundance of gut flora changed after long-term PBM irradiation.

The wavelengths of PBM were selected to be 630 nm, 730 nm, and 850 nm in this study. According to previous reports, the penetration depth of red light to infrared light in tissue was in the range of 5–10 mm (24), while the abdominal wall of mice was as thin as 1 mm. Therefore, we were confident that the energy of PBM could directly act on the intestinal flora in this study. It has been reported that PBM has a bidirectional regulation effect on bacteria. The proliferation of *E. coli* was accelerated by a 810 nm laser irradiation at 5 J/cm<sup>2</sup>, while *Pseudomonas aeruginosa* was inhibited by 23% (22). Brian Bicknell et al. found that PBM could affect intestinal flora. They irradiated the abdomen of normal mice with a laser of 808 nm for 14 days and found that the abundance of *Allobaculum* (a beneficial gut bacteria) significantly increased (25). In this study, we performed PBM for eight weeks on the abdomen of AD mice with light at wavelengths of 630 nm, 730 nm, and 850 nm. We found that intestinal flora had different responses to PBM of different wavelengths. The same responses to PBM at the three wavelengths were the opposite of the increase in *Helicobacter* and uncultured *Bacteroidales* and the decrease of *Rikenella* found in AD mice. Shen Liang et al. reported that *Helicobacter* at the genus level increased significantly in APP/PS1 mice compared with WT mice (26). In recent years, many studies have shown that *Helicobacter* infection may play an important role in AD. Beydoun MA et al. indicated that *Helicobacter* seropositivity is directly associated with AD mortality (27). Roubaud-Baudron et al. found that their *Helicobacter* infection group had a higher risk of dementia (P = 0.02) compared with the uninfected control group, and *Helicobacter* infection was identified as a risk factor for dementia (HR = 1.46) in a longitudinal study of 603 subjects aged 65 and over who were initially free of dementia and followed for 20 years (28). Therefore, we speculated that PBM irradiation to reduce the abundance of *Helicobacter pylori* in the intestinal flora might be one of the main ways to improve AD. Moreover, uncultured *Bacteroidales* and *Rikenella* are also the possible targets of PBM for AD. The wavelength of PBM has a large influence on the regulation of intestinal flora. In this study, 630 nm, 730 nm, and 850 nm PBM had unique effects on some flora as shown in Fig. 8C. All of these effects indicate the positive regulation of PBM on the dysbacteriosis of AD mice flora. These results suggest that the wavelength of PBM is an important and optimal physical parameter in future clinical applications.

The primary aim of this study was to verify whether PBM could improve the condition of AD when the intestinal flora were regulated. Cognitive behavior is the most direct clinical manifestation of AD. We found that PBM at three wavelengths (630 nm, 730 nm, and 850 nm) can effectively improve the impaired learning ability of AD mice, but it affected memory ability to a lesser extent (Fig. 2). The hippocampus is responsible for functions such as storage conversion and orientation in long-term memory. The hippocampus is essential to spatial navigation via a cognitive map, which is not dedicated to spatial cognition and navigation, but organizes experiences in memory. Justin D. Shin et al. also showed that the hippocampal-prefrontal region not only contributes to spatial learning, but also to memory-guided decision making (29). In our study, PBM improved the learning ability of AD mice but not the memory ability of mice, indicating that PBM could not completely repair the hippocampal networks. It is possible that our study needed a longer irradiation time or optimized conditions of PBM to observe memory improvement.

Amyloid plaques, tau phosphorylation, and neuroinflammation are the main pathological changes of AD (4). We found that mice in the PBM groups showed amyloid plaque elimination, p-tau reduction, and microglia proliferation. In addition, the PBM intervention resulted in a large number of proteins up- or downregulated in the hippocampus of AD mice (Fig. 5). Most of these common DEPs are involved in hormone secretion and inflammatory responses (Fig. 7), which are the main pathways by which the intestinal flora may affect AD (7). In the molecular pathway of AD, key proteins in the mitochondrial respiratory chain complex enzyme are up- or downregulated and tau protein is significantly decreased. Mesenteric immunity is an important part of the body's total immunity, and it is also the tissue most likely exposed to PBM during abdominal PBM treatment. However, our results showed that PBM did not significantly increase the proliferation of lymphocytes and macrophages in the mesenteric lymph nodes except for the increase in mesenteric blood flow (Fig. 4). This suggests that cellular immunity does not participate in gf-targeted PBM. However, in humoral immunity, we found that INF- $\gamma$  was significantly increased after PBM irradiation, especially for PBM630 and PBM730. It has been reported that the metabolites of intestinal flora can increase the serum levels of inflammatory factors such as IL-1 $\alpha$ , IL-6, IL-10, TNF- $\alpha$ , and INF- $\gamma$ , and promote the hyperphosphorylation of tau proteins and the excessive activation of microglia through the blood-brain barrier (30). In our A $\beta_{1-42}$ -induced AD mice, IL-6 and INF were both at a lower level compared with the normal mice. PBM did not increase IL-6 levels, but it significantly increased INF levels. We believe that this is due to the selective regulation of intestinal flora by PBM.

## Limitations

First, A $\beta$ -induced AD mice is a simple AD model which simulates the main pathological features of AD patients through the deposition of exogenous A $\beta_{1-42}$  proteins in the hippocampus. Other causes of AD are not reflected in this model, so we will attempt to verify these results in two or more AD models in future studies. Second, the modeling time was short. The PBM intervention started 2 weeks after modeling, although the intestinal flora of AD mice was significantly altered at the end point (10 weeks after modeling) compared to the control group. The causal relationship between intestinal flora and AD is relatively complex, but in this experiment, it was artificially assumed that AD pathological changes would first cause intestinal flora abnormalities. Future studies will gather more evidence to verify the effect of PBM on AD and intestinal flora. Finally, although we found that *Helicobacter pylori* may be the dominant PBM regulatory flora, sufficient single-factor validation was still lacking.

## Conclusions

In conclusion, gf-targeted PBM with light at 630 nm, 730 nm, and 850 nm reversed the imbalance of intestinal flora and improved learning ability, amyloid plaque deposition, tau phosphorylation, and microglia inflammation of A $\beta$ -induced AD mice. A large number of proteins in the hippocampus responded to gf-targeted PBM, with mitochondrial respiratory chain complex enzymes as a possible key intermediate target. In future studies, we will confirm the effect of gf-targeted PBM on the brain-gut axis in

additional AD animal models, such as APP/PS1 double-transgenic mice, and fully verify the targeted flora of PBM, which will promote PBM as a potential prevention and treatment method for AD.

## Abbreviations

AD: Alzheimer's disease; PBM: Photobiomodulation; gf-targeted PBM: gut flora-targeted PBM; A $\beta$ : Amyloid- $\beta$ ; TMT: tandem mass tags; DEPs: differentially expression proteins; MWM: Morris water maze

## Declarations

### Acknowledgments

We thank Korin Albert, PhD, from Liwen Bianji, Edanz Editing China ([www.liwenbianji.cn/ac](http://www.liwenbianji.cn/ac)), for editing the English text of a draft of this manuscript.

### Authors' contributions

Qianqian Chen performed the primary animal experiments. Jinpeng Wu analyzed the proteomics data. Xiaoxi Dong made the light devices for the animal experiments. Xiafei Shi and Bochen Che helped to perform the animal experiments. Siying Su assisted in immunofluorescence. Huijuan Yin wrote the manuscript and Yingxin Li edited the manuscript.

### Funding

This work was supported by the National Key Research and Development Program "Study on optical parameter research, equipment development and demonstration application of LED treatment of skin diseases" (No. 2017YFB0403804).

### Availability of data and materials

All data generated or analyzed during this study are included in this published article.

### Ethics approval and consent to participate

All experimental protocols involving rats were approved by the animal ethics and welfare committee (approval number: IRM-DWLL-2018125) of the Institute of Radiation Medicine, Chinese Academy of Medical Sciences, Tianjin, China.

### Consent for publication

All authors have approved of the manuscript and agree with its submission

### Competing interests

The authors declare that they have no competing interests.

## References

1. Herrup K. Reimagining Alzheimer's disease—an age-based hypothesis. *J Neurosci*. 2010;30(50):16755–62.
2. World. Alzheimer Report 2018.
3. Brody H. Alzheimer's disease. *Nature*. 2011;475(7355):1.
4. Hodson R. Alzheimer's disease. *Nature*. 2018;559(7715):1.
5. Musardo S, Saraceno C, Pelucchi S, Marcello E. Trafficking in neurons: searching for new targets for Alzheimer's disease future therapies. *Eur J Pharmacol*. 2013;719(1–3):84–106.
6. Stower H. Searching for Alzheimer's disease therapies. *Nat Med*. 2018;24(7):894–7.
7. Khan MS, Ikram M, Park JS, Park TJ, Kim MO. Gut Microbiota, Its Role in Induction of Alzheimer's Disease Pathology, and Possible Therapeutic Interventions: Special Focus on Anthocyanins. *Cells*. 2020;9(4).
8. Pluta R, Ulamek-Kozioł M, Januszewski S, Czuczwar SJ. Gut microbiota and pro/prebiotics in Alzheimer's disease. *Aging*. 2020;12(6):5539–50.
9. Kong Y, Jiang B, Luo X. Gut microbiota influences Alzheimer's disease pathogenesis by regulating acetate in *Drosophila* model. *Future Microbiol*. 2018;13:1117–28.
10. Giau VV, Wu SY, Jamerlan A, An SSA, Kim SY, Hulme J. Gut Microbiota and Their Neuroinflammatory Implications in Alzheimer's Disease. *Nutrients*. 2018;10(11).
11. Woo JY, Gu W, Kim KA, Jang SE, Han MJ, Kim DH. *Lactobacillus pentosus* var. *plantarum* C29 ameliorates memory impairment and inflammaging in a D-galactose-induced accelerated aging mouse model. *Anaerobe*. 2014;27:22–6.
12. Akbari E, Asemi Z, Daneshvar Kakhaki R, Bahmani F, Kouchaki E, Tamtaji OR, et al. Effect of Probiotic Supplementation on Cognitive Function and Metabolic Status in Alzheimer's Disease: A Randomized, Double-Blind and Controlled Trial. *Front Aging Neurosci*. 2016;8:256.
13. Chung H, Dai T, Sharma SK, Huang YY, Carroll JD, Hamblin MR. The nuts and bolts of low-level laser (light) therapy. *Ann Biomed Eng*. 2012;40(2):516–33.
14. Salehpour F, Mahmoudi J, Kamari F, Sadigh-Eteghad S, Rasta SH, Hamblin MR. Brain Photobiomodulation Therapy: a Narrative Review. *Mol Neurobiol*. 2018;55(8):6601–36.
15. Hamblin MR. Mechanisms and Mitochondrial Redox Signaling in Photobiomodulation. *Photochem Photobiol*. 2018;94(2):199–212.
16. de Freitas LF, Hamblin MR. Proposed Mechanisms of Photobiomodulation or Low-Level Light Therapy. *IEEE J Sel Top Quantum Electron*. 2016;22(3).
17. Karu T. Mitochondrial mechanisms of photobiomodulation in context of new data about multiple roles of ATP. *Photomed Laser Surg*. 2010;28(2):159–60.
18. Salehpour F, Rasta SH. The potential of transcranial photobiomodulation therapy for treatment of major depressive disorder. *Rev Neurosci*. 2017;28(4):441–53.

19. Hong N. Photobiomodulation as a treatment for neurodegenerative disorders: current and future trends. *Biomed Eng Lett*. 2019;9(3):359–66.
20. Percival SL, Francolini I, Donelli G. Low-level laser therapy as an antimicrobial and antibiofilm technology and its relevance to wound healing. *Future Microbiol*. 2015;10(2):255–72.
21. Guffey JS, Wilborn J. In vitro bactericidal effects of 405-nm and 470-nm blue light. *Photomed Laser Surg*. 2006;24(6):684–8.
22. Nussbaum EL, Lilge L, Mazzulli T. Effects of 630-, 660-, 810-, and 905-nm laser irradiation delivering radiant exposure of 1–50 J/cm<sup>2</sup> on three species of bacteria in vitro. *J Clin Laser Med Surg*. 2002;20(6):325–33.
23. Wang Q, Garrity GM, Tiedje JM, Cole JR. Naive Bayesian classifier for rapid assignment of rRNA sequences into the new bacterial taxonomy. *Appl Environ Microbiol*. 2007;73(16):5261–7.
24. Agostinis P, Berg K, Cengel KA, Foster TH, Girotti AW, Gollnick SO, et al. Photodynamic therapy of cancer: an update. *CA Cancer J Clin*. 2011;61(4):250–81.
25. Bicknell B, Liebert A, Johnstone D, Kiat H. Photobiomodulation of the microbiome: implications for metabolic and inflammatory diseases. *Lasers Med Sci*. 2019;34(2):317–27.
26. Shen L, Liu L, Ji HF. Alzheimer's Disease Histological and Behavioral Manifestations in Transgenic Mice Correlate with Specific Gut Microbiome State. *J Alzheimers Dis*. 2017;56(1):385–90.
27. Beydoun MA, Beydoun HA, Elbejjani M, Dore GA, Zonderman AB. Helicobacter pylori seropositivity and its association with incident all-cause and Alzheimer's disease dementia in large national surveys. *Alzheimers Dement*. 2018;14(9):1148–58.
28. Roubaud Baudron C, Letenneur L, Langlais A, Buissonnière A, Mégraud F, Dartigues JF, et al. Does Helicobacter pylori infection increase incidence of dementia? The Personnes Agées QUID Study. *J Am Geriatr Soc*. 2013;61(1):74–8.
29. Shin JD, Tang W, Jadhav SP. Dynamics of Awake Hippocampal-Prefrontal Replay for Spatial Learning and Memory-Guided Decision Making. *Neuron*. 2019;104(6):1110–25.e7.
30. Savignac HM, Couch Y, Stratford M, Bannerman DM, Tzortzis G, Anthony DC, et al. Prebiotic administration normalizes lipopolysaccharide (LPS)-induced anxiety and cortical 5-HT<sub>2A</sub> receptor and IL1-beta levels in male mice. *Brain Behav Immun*. 2016;52:120–31.

## Figures

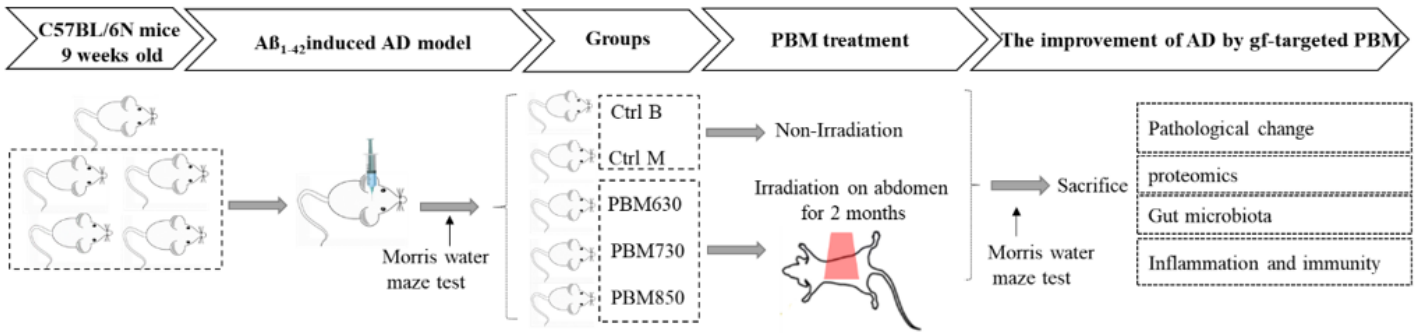


**Figure 1**

Scheme for the study of gut flora-targeted (gf-targeted) photobiomodulation (PBM) treatment on Alzheimer's disease (AD) mice.

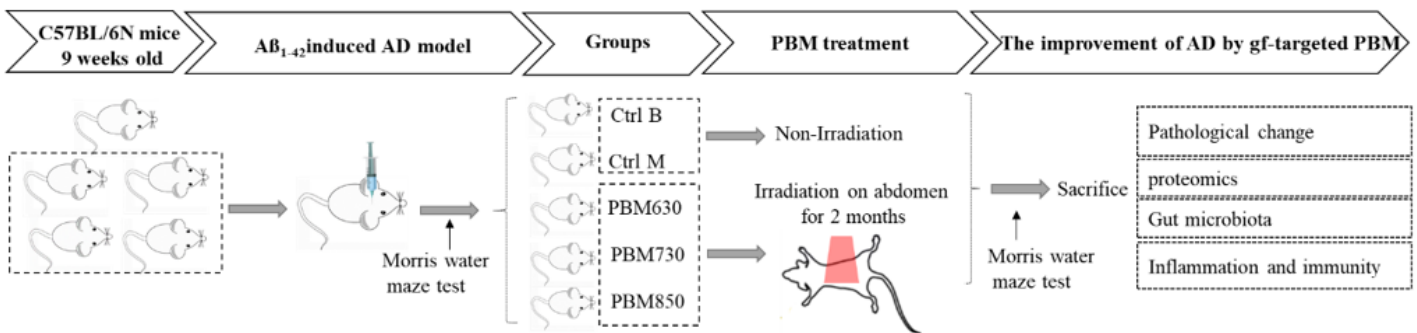


**Figure 1**

Scheme for the study of gut flora-targeted (gf-targeted) photobiomodulation (PBM) treatment on Alzheimer's disease (AD) mice.

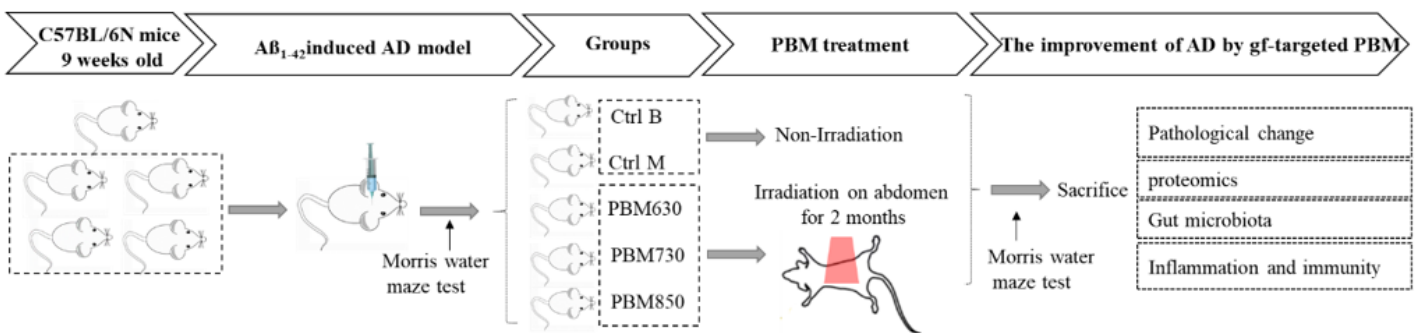


**Figure 1**

Scheme for the study of gut flora-targeted (gf-targeted) photobiomodulation (PBM) treatment on Alzheimer's disease (AD) mice.

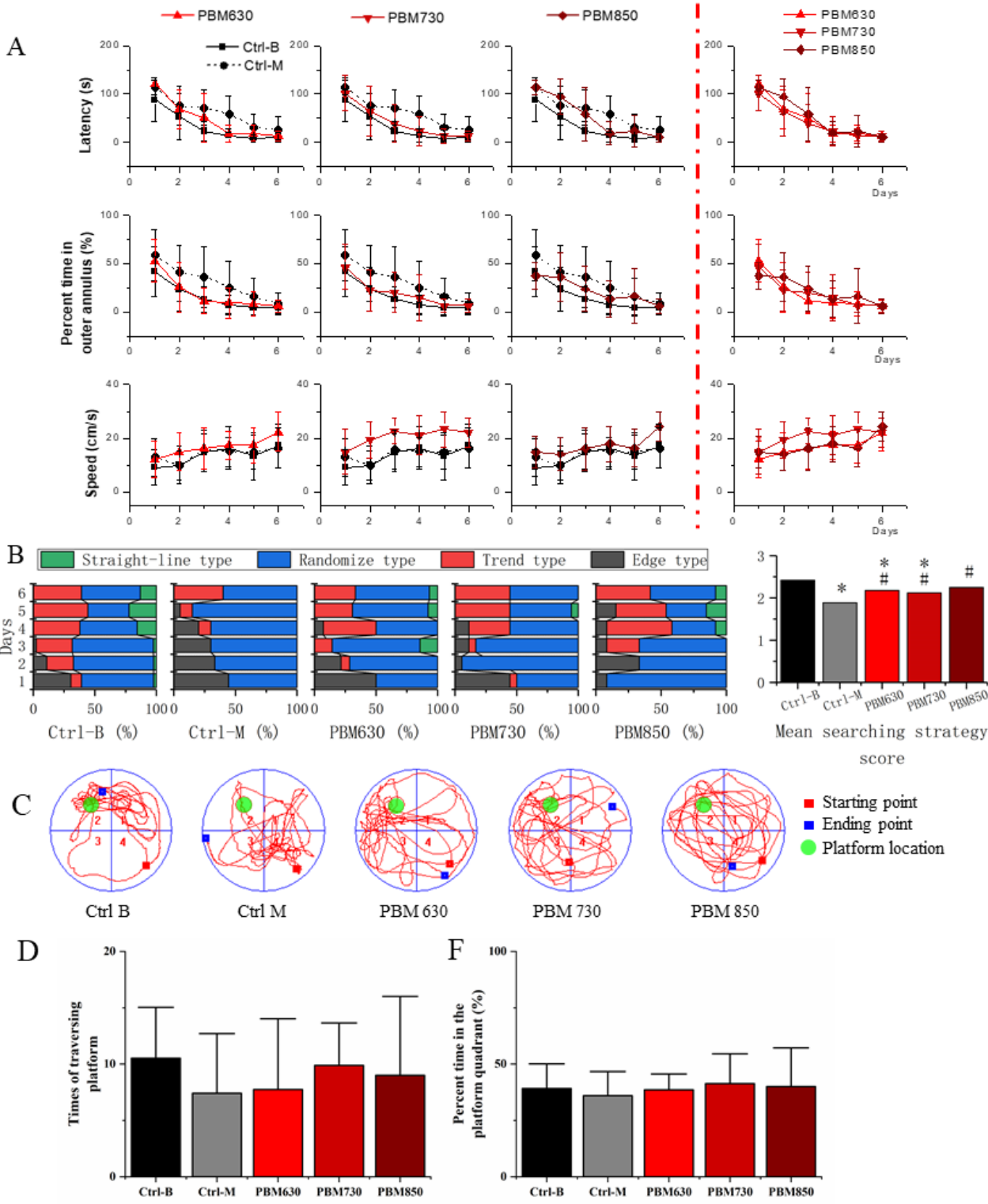


**Figure 2**

Learning and memory ability of Alzheimer’s disease (AD) mice after photobiomodulation (PBM) intervention. A. The escape latency, percent time in the outer annulus, and swimming speed of the AD mice treated with PBM630, PBM730, and PBM850 compared with the normal and AD control mice in a Morris water maze (MWM) test. The comparisons between the three PBM groups were extracted from the

left graph. B. The searching strategy graph (left percentage chart) and scores (right histogram) of the AD mice treated with PBM in a MWM test.

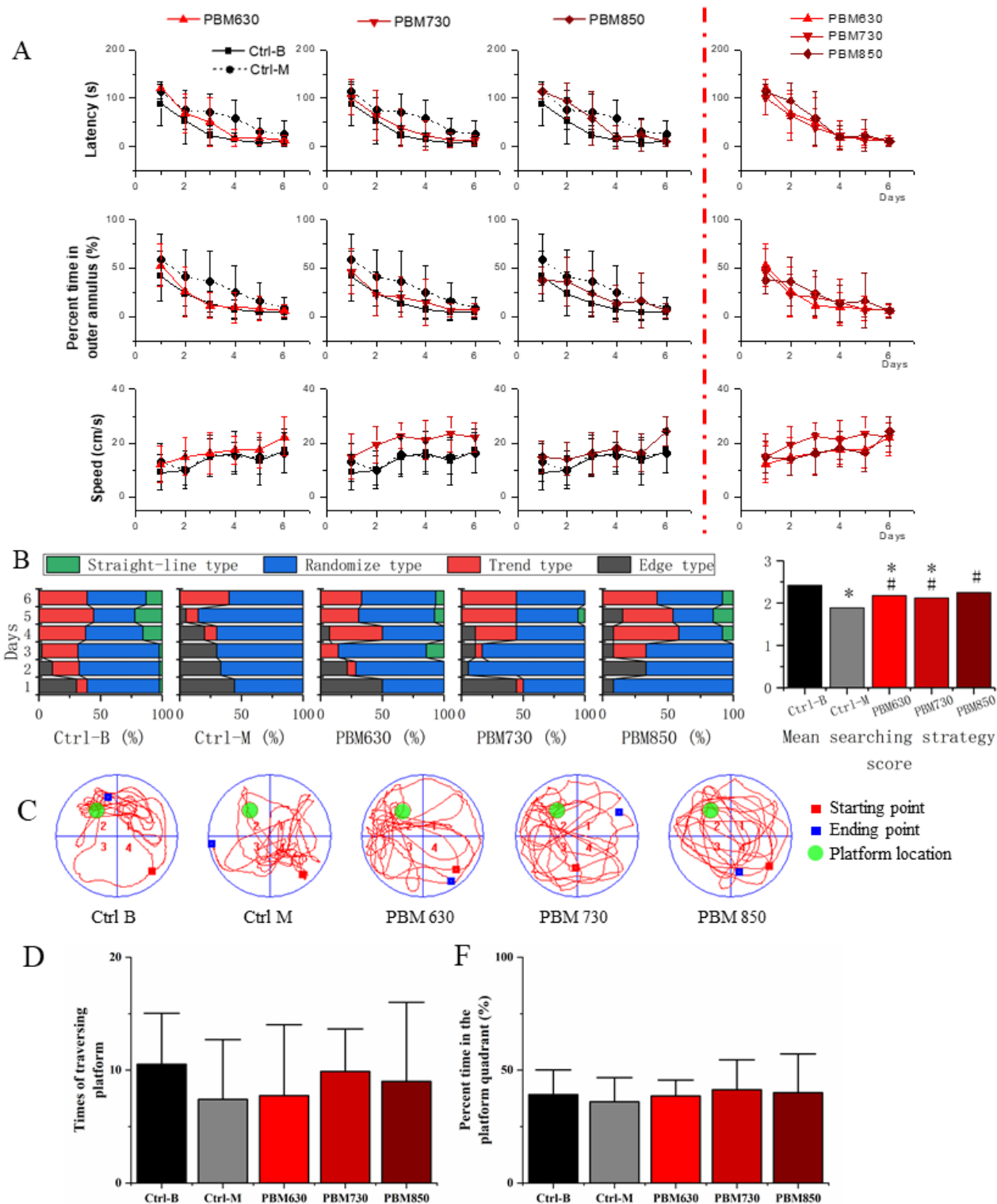


**Figure 2**

Learning and memory ability of Alzheimer’s disease (AD) mice after photobiomodulation (PBM) intervention. A. The escape latency, percent time in the outer annulus, and swimming speed of the AD mice treated with PBM630, PBM730, and PBM850 compared with the normal and AD control mice in a

Morris water maze (MWM) test. The comparisons between the three PBM groups were extracted from the left graph. B. The searching strategy graph (left percentage chart) and scores (right histogram) of the AD mice treated with PBM in a MWM test.

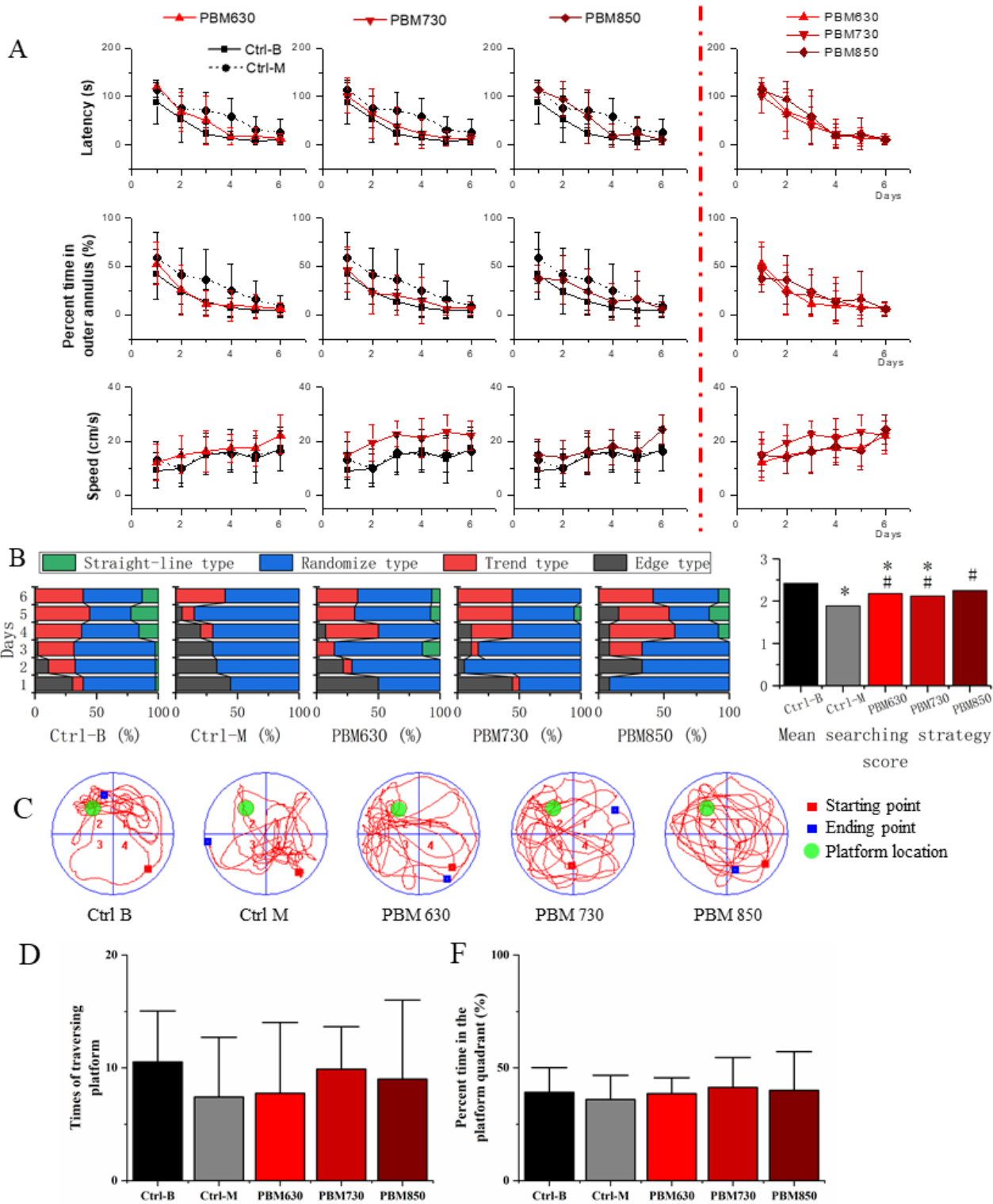


**Figure 2**

Learning and memory ability of Alzheimer's disease (AD) mice after photobiomodulation (PBM) intervention. A. The escape latency, percent time in the outer annulus, and swimming speed of the AD

mice treated with PBM630, PBM730, and PBM850 compared with the normal and AD control mice in a Morris water maze (MWM) test. The comparisons between the three PBM groups were extracted from the left graph. B. The searching strategy graph (left percentage chart) and scores (right histogram) of the AD mice treated with PBM in a MWM test.

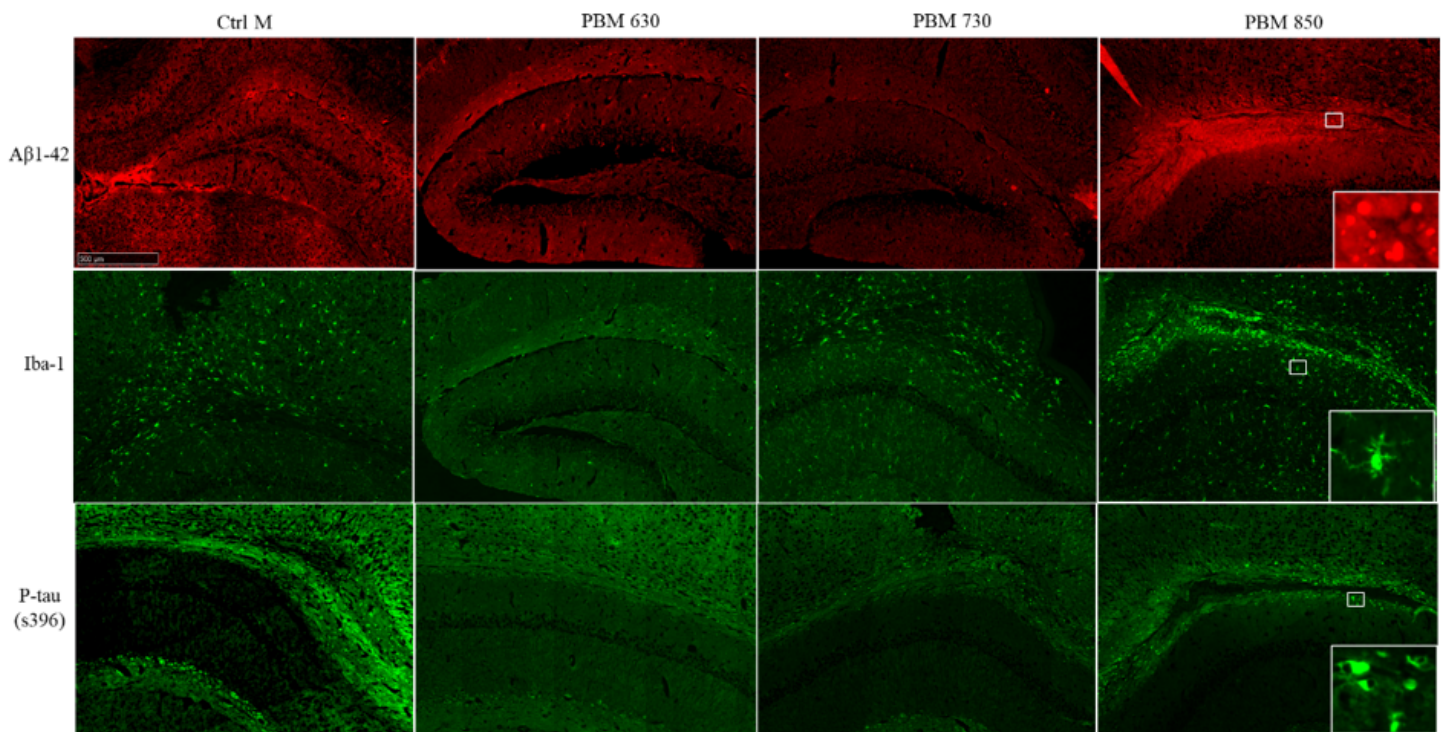


**Figure 3**

Improvement of Alzheimer's disease (AD) pathology induced by irradiation of photobiomodulation (PBM) in AD mice. The main images are shown in 5x magnification, and the inserted images (white box) in the right column images were taken at 40x magnification. The frozen sections of hippocampus from the mice in the Ctrl M, PBM630, PBM730, and PBM850 groups were sliced 50  $\mu$ m thick and stained by the primary antibodies A $\beta$ 1-42, Iba1, and p-tau(s396) and the second antibodies of Rhodamine (TRITC) IgG and Alexa Fluor® 488 IgG.

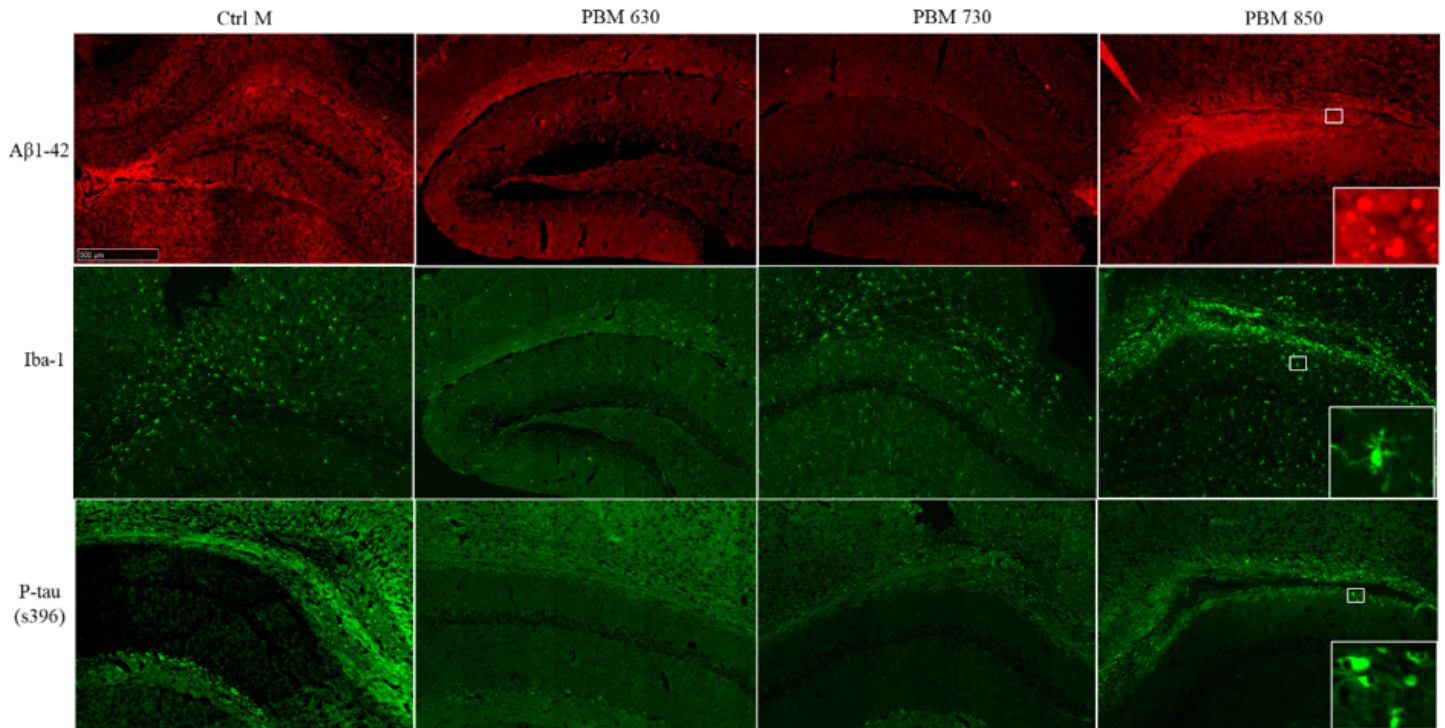


**Figure 3**

Improvement of Alzheimer's disease (AD) pathology induced by irradiation of photobiomodulation (PBM) in AD mice. The main images are shown in 5x magnification, and the inserted images (white box) in the right column images were taken at 40x magnification. The frozen sections of hippocampus from the mice in the Ctrl M, PBM630, PBM730, and PBM850 groups were sliced 50  $\mu$ m thick and stained by the primary antibodies A $\beta$ 1-42, Iba1, and p-tau(s396) and the second antibodies of Rhodamine (TRITC) IgG and Alexa Fluor® 488 IgG.

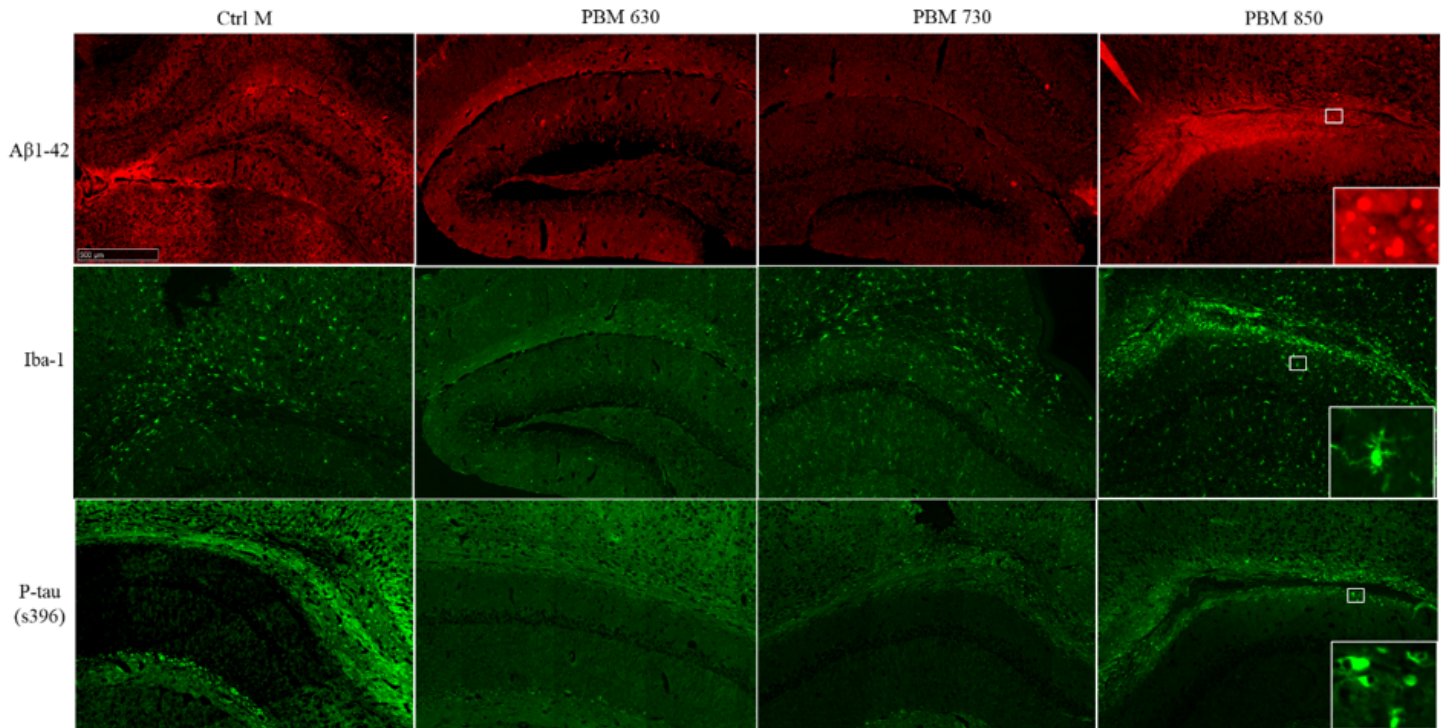


**Figure 3**

Improvement of Alzheimer's disease (AD) pathology induced by irradiation of photobiomodulation (PBM) in AD mice. The main images are shown in 5x magnification, and the inserted images (white box) in the right column images were taken at 40x magnification. The frozen sections of hippocampus from the mice in the Ctrl M, PBM630, PBM730, and PBM850 groups were sliced 50  $\mu$ m thick and stained by the primary antibodies A $\beta$ 1-42, Iba1, and p-tau(s396) and the second antibodies of Rhodamine (TRITC) IgG and Alexa Fluor® 488 IgG.

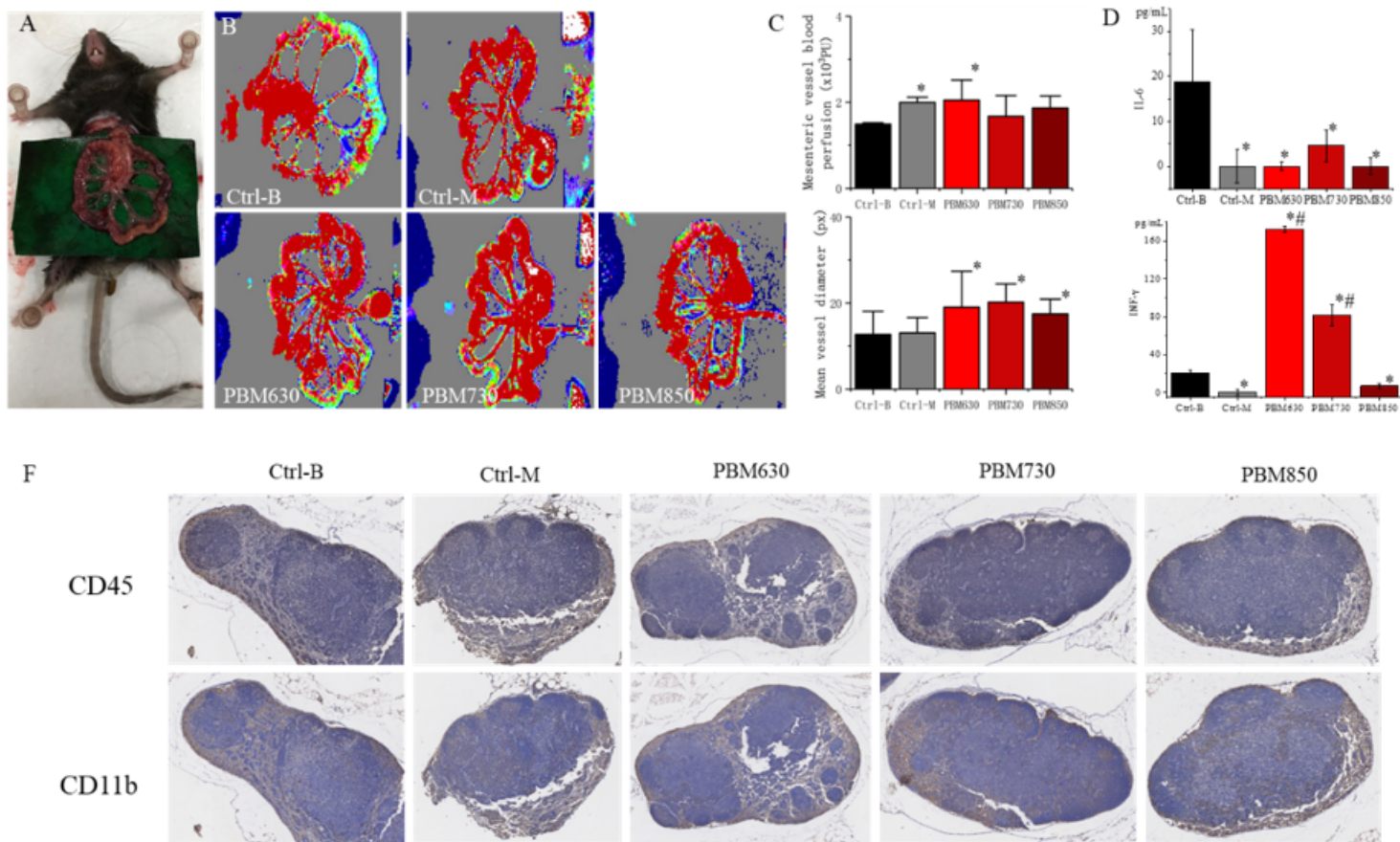


**Figure 4**

Effects of photobiomodulation (PBM) treatment on mesenteric blood flow and the immune system. A. Sample preparation before laser speckle detection (mesentery and small intestine) under anesthesia. B. The intensity map of blood flow acquired from the laser speckle. C. The vessel blood perfusion and mean vessel diameter calculated from B. D. The level of proinflammatory cytokines IL-6 and INF- $\gamma$  in the serum of mice. An asterisk (\*) denotes a significant difference ( $p < 0.05$ ) compared with Ctrl B, and a hashtag (#) denotes a significant difference ( $p < 0.05$ ) compared with Ctrl M. F. Immunostaining for CD45 (marker for leukocytes) and CD11b (marker for phagocytes) in mesenteric lymph nodes.

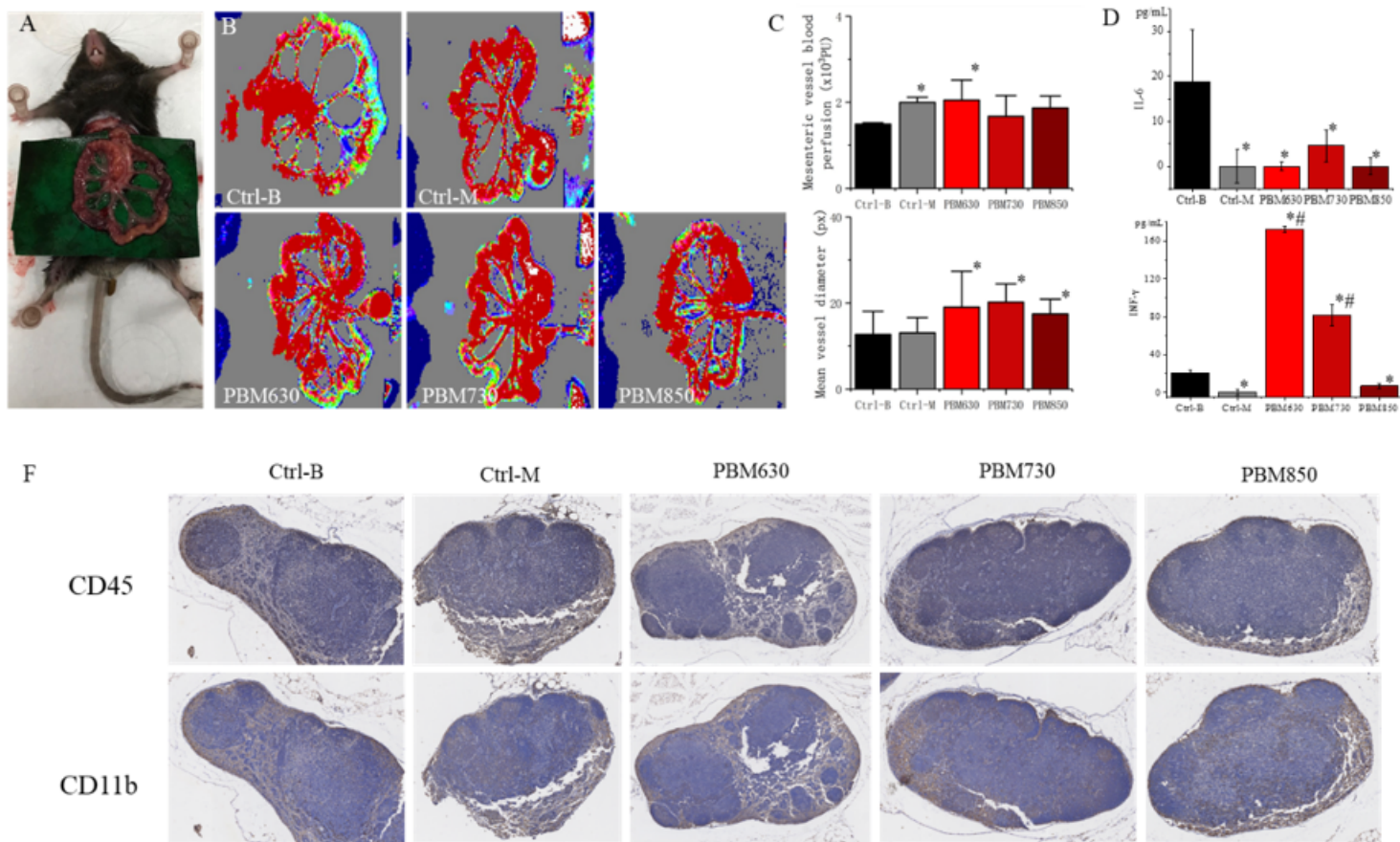


**Figure 4**

Effects of photobiomodulation (PBM) treatment on mesenteric blood flow and the immune system. A. Sample preparation before laser speckle detection (mesentery and small intestine) under anesthesia. B. The intensity map of blood flow acquired from the laser speckle. C. The vessel blood perfusion and mean vessel diameter calculated from B. D. The level of proinflammatory cytokines IL-6 and INF- $\gamma$  in the serum of mice. An asterisk (\*) denotes a significant difference ( $p < 0.05$ ) compared with Ctrl B, and a hashtag (#) denotes a significant difference ( $p < 0.05$ ) compared with Ctrl M. F. Immunostaining for CD45 (marker for leukocytes) and CD11b (marker for phagocytes) in mesenteric lymph nodes.

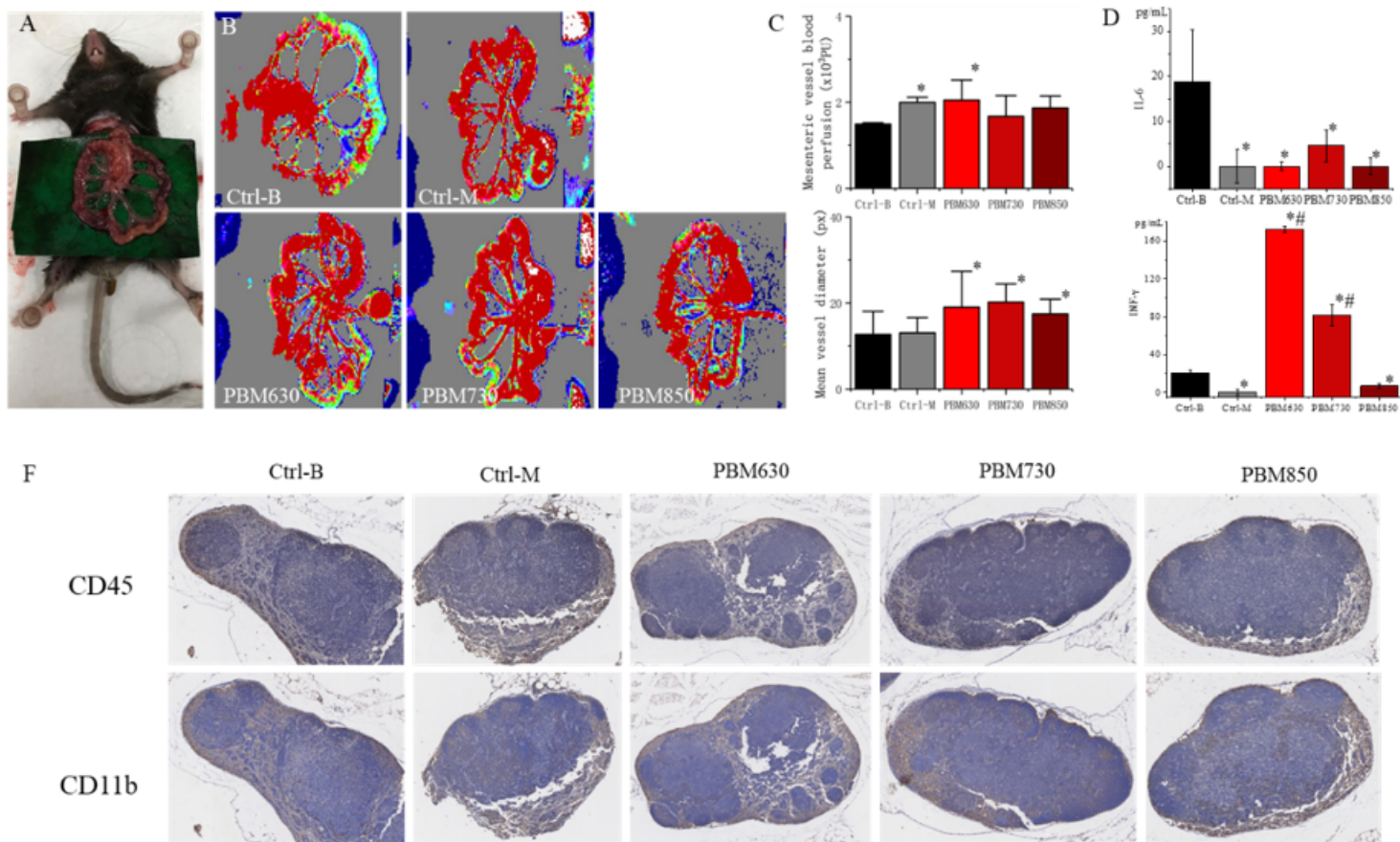


**Figure 4**

Effects of photobiomodulation (PBM) treatment on mesenteric blood flow and the immune system. A. Sample preparation before laser speckle detection (mesentery and small intestine) under anesthesia. B. The intensity map of blood flow acquired from the laser speckle. C. The vessel blood perfusion and mean vessel diameter calculated from B. D. The level of proinflammatory cytokines IL-6 and INF- $\gamma$  in the serum of mice. An asterisk (\*) denotes a significant difference ( $p < 0.05$ ) compared with Ctrl B, and a hashtag (#) denotes a significant difference ( $p < 0.05$ ) compared with Ctrl M. F. Immunostaining for CD45 (marker for leukocytes) and CD11b (marker for phagocytes) in mesenteric lymph nodes.

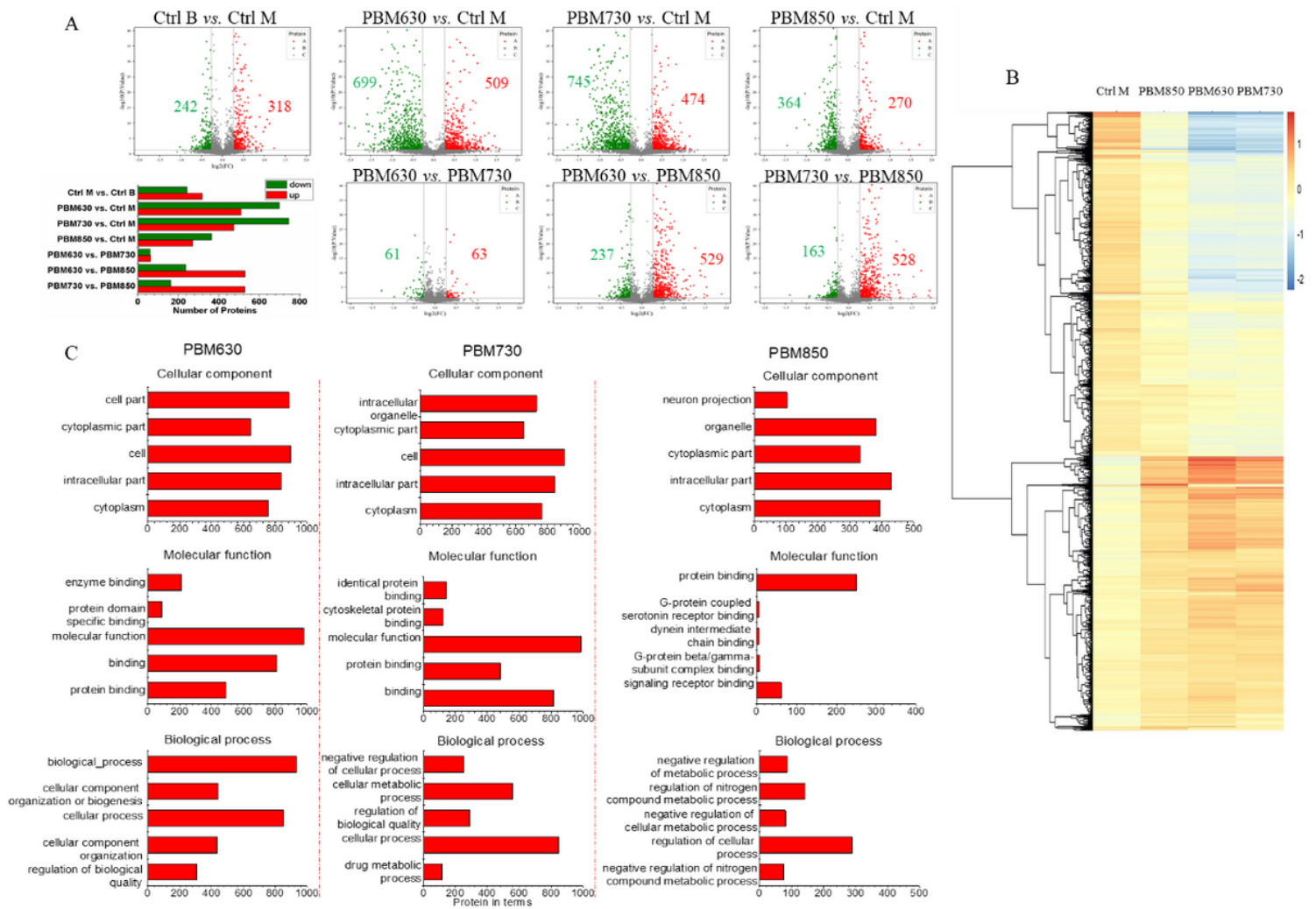


**Figure 5**

Overview of differentially expressed protein (DEP) and GO analyses in hippocampal tissues of paired comparisons among five groups, including Ctrl B, Ctrl M, PBM630, PBM730, and PBM850. A. The volcano plots in the first row represent the DEPs in Ctrl B, PBM630, PBM730, and PBM850 compared with Ctrl M. The volcano plots in the second row represent the DEPs of paired comparisons among the three PBM groups. The red dots are upregulated DEPs and the green dots are downregulated DEPs. The inverted histogram shows the upregulated and downregulated DEPs from the seven volcano maps. B. The heat map shows the cluster analysis of DEPs of the paired comparisons of Ctrl M to Ctrl B and PBM630, PBM730, and PBM850 to Ctrl M. C. GO analysis of DEPs of PBM630, PBM730, and PBM850 compared with Ctrl M. The five proteins with the lowest p values in the classification of cell composition, molecular function, and biological processes are listed.

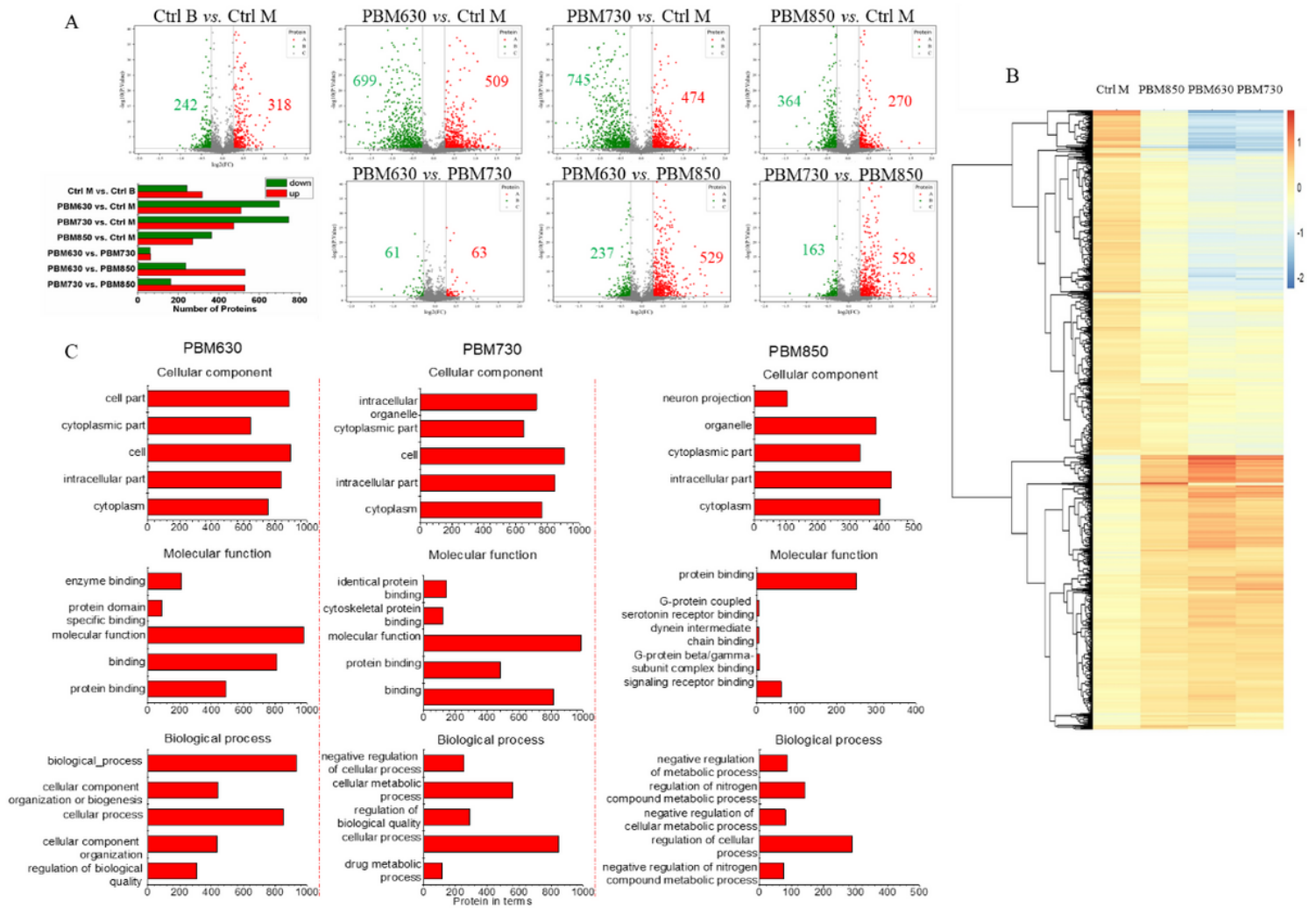


**Figure 5**

Overview of differentially expressed protein (DEP) and GO analyses in hippocampal tissues of paired comparisons among five groups, including Ctrl B, Ctrl M, PBM630, PBM730, and PBM850. A. The volcano plots in the first row represent the DEPs in Ctrl B, PBM630, PBM730, and PBM850 compared with Ctrl M. The volcano plots in the second row represent the DEPs of paired comparisons among the three PBM groups. The red dots are upregulated DEPs and the green dots are downregulated DEPs. The inverted histogram shows the upregulated and downregulated DEPs from the seven volcano maps. B. The heat map shows the cluster analysis of DEPs of the paired comparisons of Ctrl M to Ctrl B and PBM630, PBM730, and PBM850 to Ctrl M. C. GO analysis of DEPs of PBM630, PBM730, and PBM850 compared with Ctrl M. The five proteins with the lowest p values in the classification of cell composition, molecular function, and biological processes are listed.

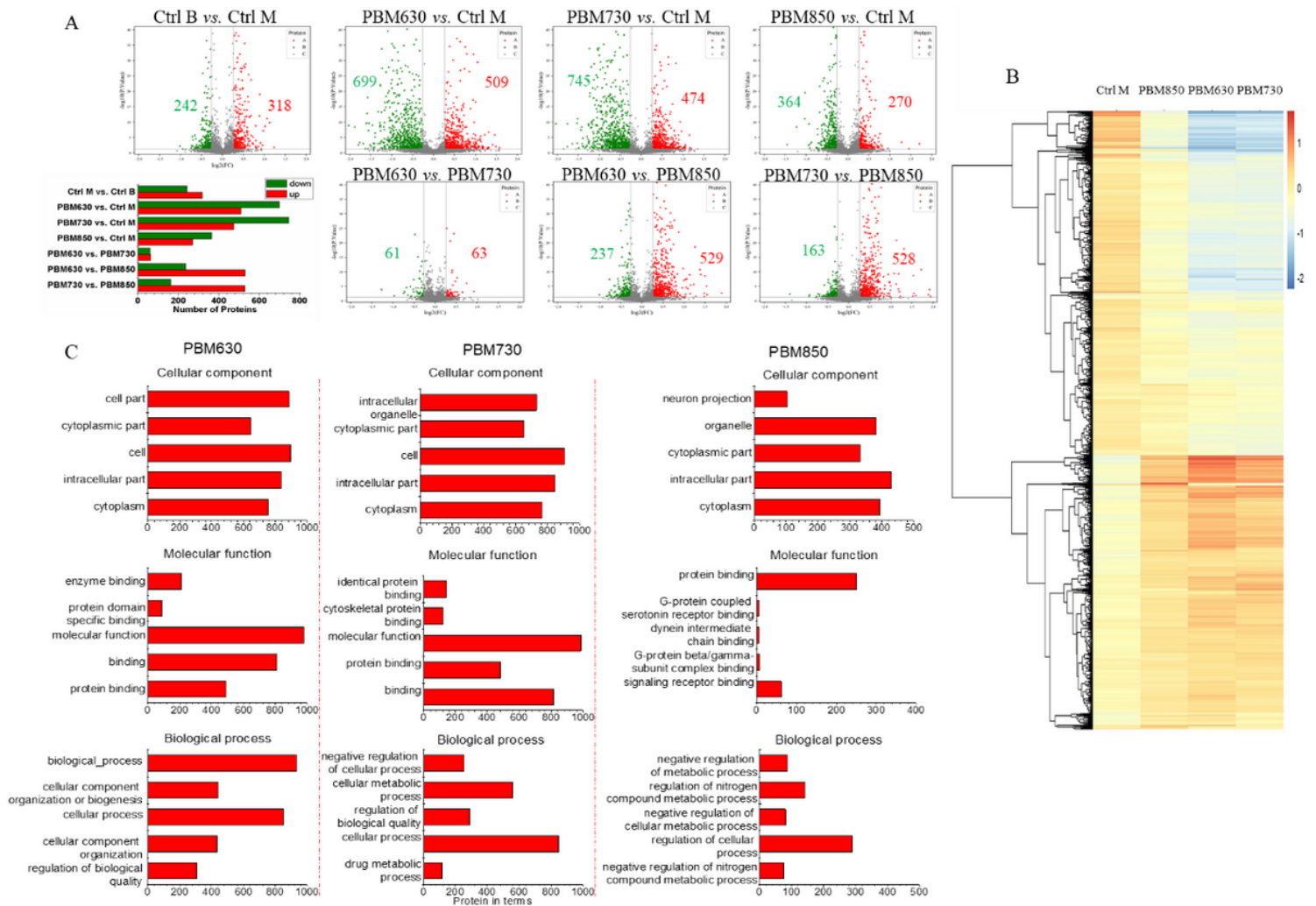


**Figure 5**

Overview of differentially expressed protein proteins (DEP) and GO analyses in hippocampal tissues of paired comparisons among five groups, including Ctrl B, Ctrl M, PBM630, PBM730, and PBM850. A. The volcano plots in the first row represent the DEPs in Ctrl B, PBM630, PBM730, and PBM850 compared with Ctrl M. The volcano plots in the second row represent the DEPs of paired comparisons among the three PBM groups. The red dots are upregulated DEPs and the green dots are downregulated DEPs. The inverted histogram shows the upregulated and downregulated DEPs from the seven volcano maps. B. The heat map shows the cluster analysis of DEPs of the paired comparisons of Ctrl M to Ctrl B and PBM630, PBM730, and PBM850 to Ctrl M. C. GO analysis of DEPs of PBM630, PBM730, and PBM850 compared with Ctrl M. The five proteins with the lowest p values in the classification of cell composition, molecular function, and biological processes are listed.

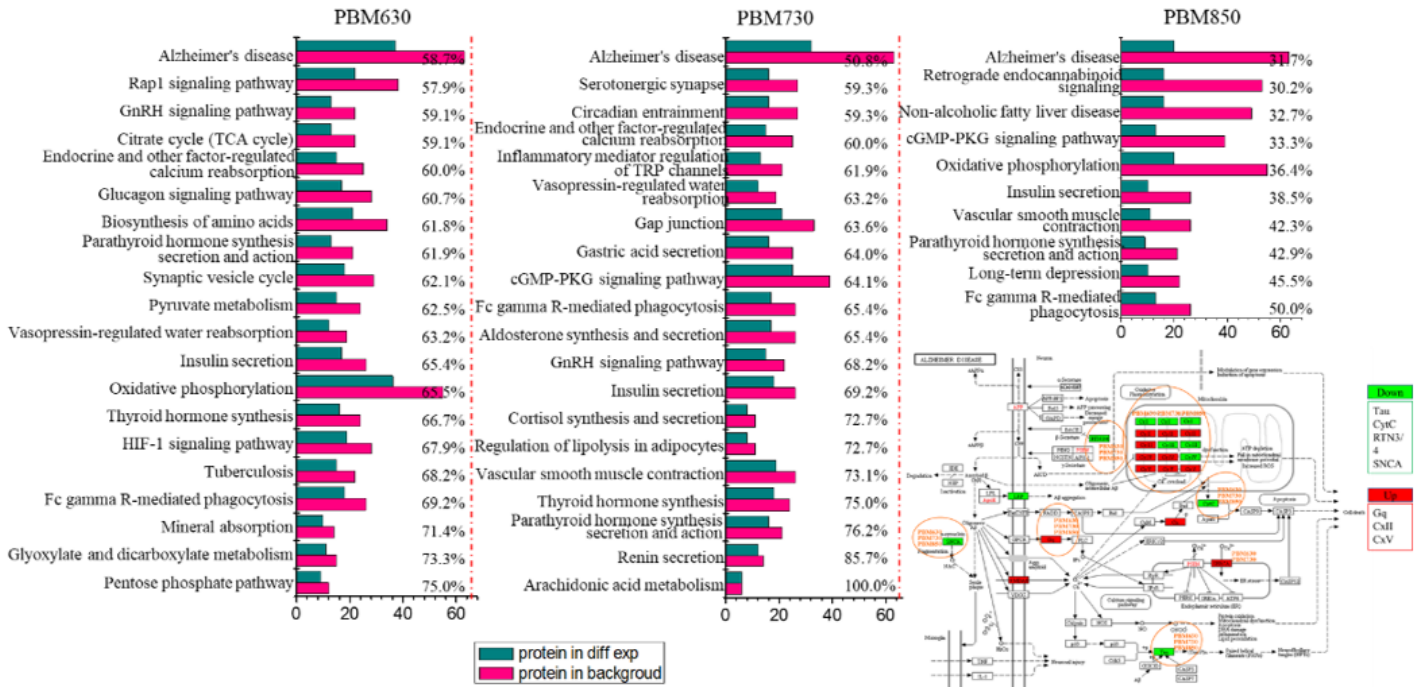


**Figure 6**

KEGG pathway analysis of differentially expressed proteins (DEP) of PBM630, PBM730, and PBM850 compared with Ctrl M. The pathways with p values of less than 0.05 were removed, and the remaining pathways were sorted according to the ratio of DEPs to background proteins. The blue bars represent the DEPs involved in the pathway, and the red bars represent the total proteins involved in a pathway. The percentages located on the right of the histogram are the ratios of the numbers of DEPs in each pathway to the number of background proteins in that pathway.

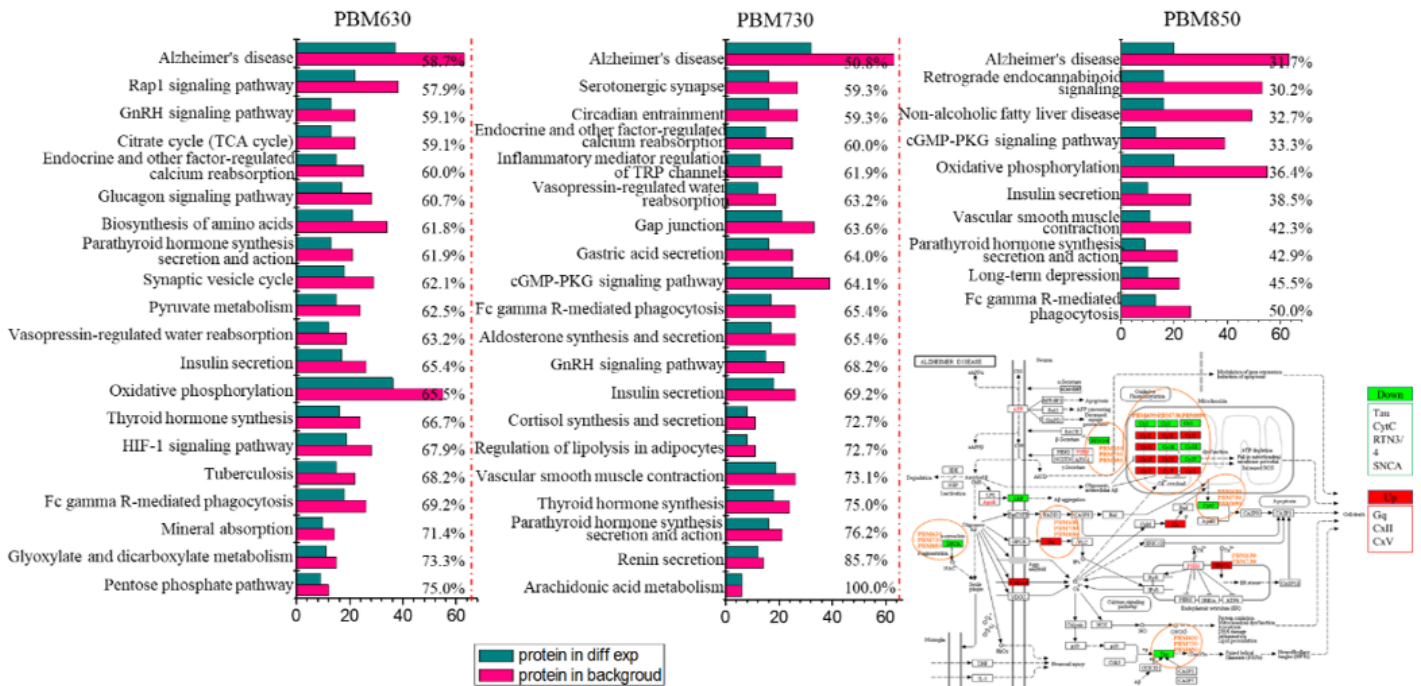


**Figure 6**

KEGG pathway analysis of differentially expressed proteins (DEP) of PBM630, PBM730, and PBM850 compared with Ctrl M. The pathways with p values of less than 0.05 were removed, and the remaining pathways were sorted according to the ratio of DEPs to background proteins. The blue bars represent the DEPs involved in the pathway, and the red bars represent the total proteins involved in a pathway. The percentages located on the right of the histogram are the ratios of the numbers of DEPs in each pathway to the number of background proteins in that pathway.

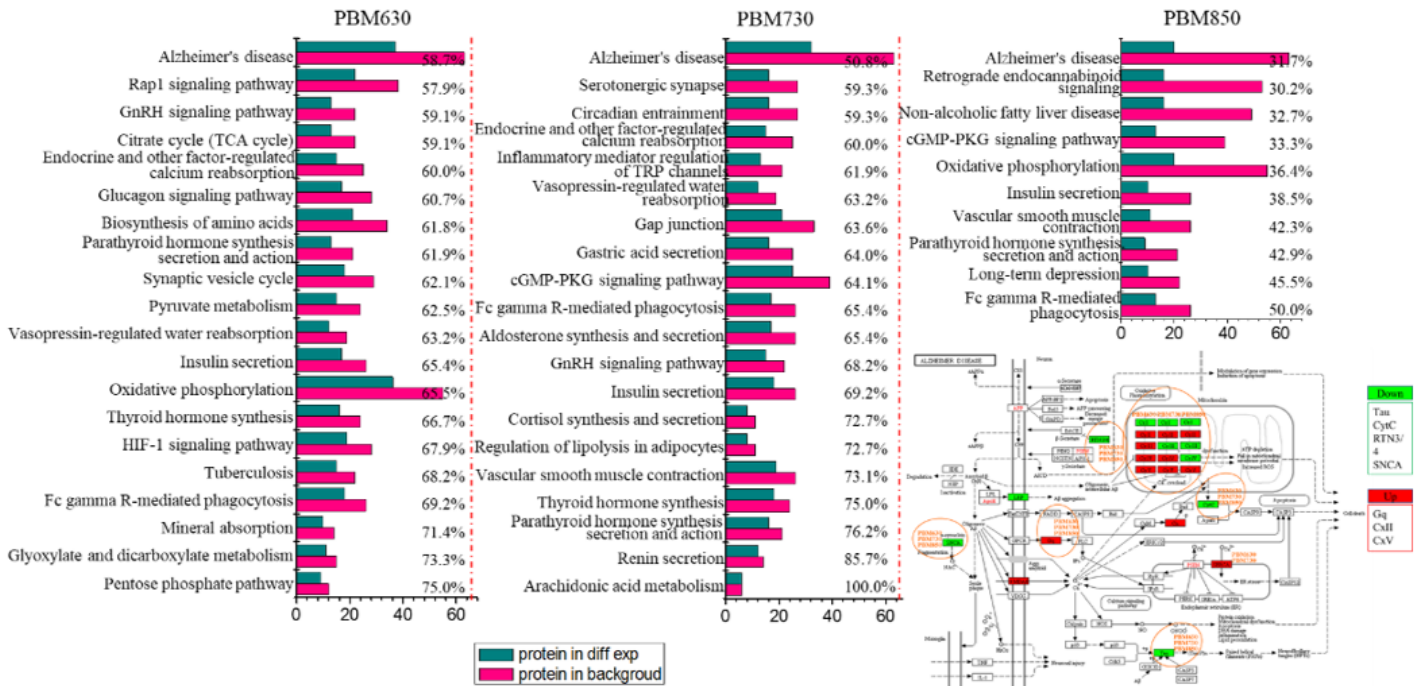


**Figure 6**

KEGG pathway analysis of differentially expressed proteins (DEP) of PBM630, PBM730, and PBM850 compared with Ctrl M. The pathways with p values of less than 0.05 were removed, and the remaining pathways were sorted according to the ratio of DEPs to background proteins. The blue bars represent the DEPs involved in the pathway, and the red bars represent the total proteins involved in a pathway. The percentages located on the right of the histogram are the ratios of the numbers of DEPs in each pathway to the number of background proteins in that pathway.

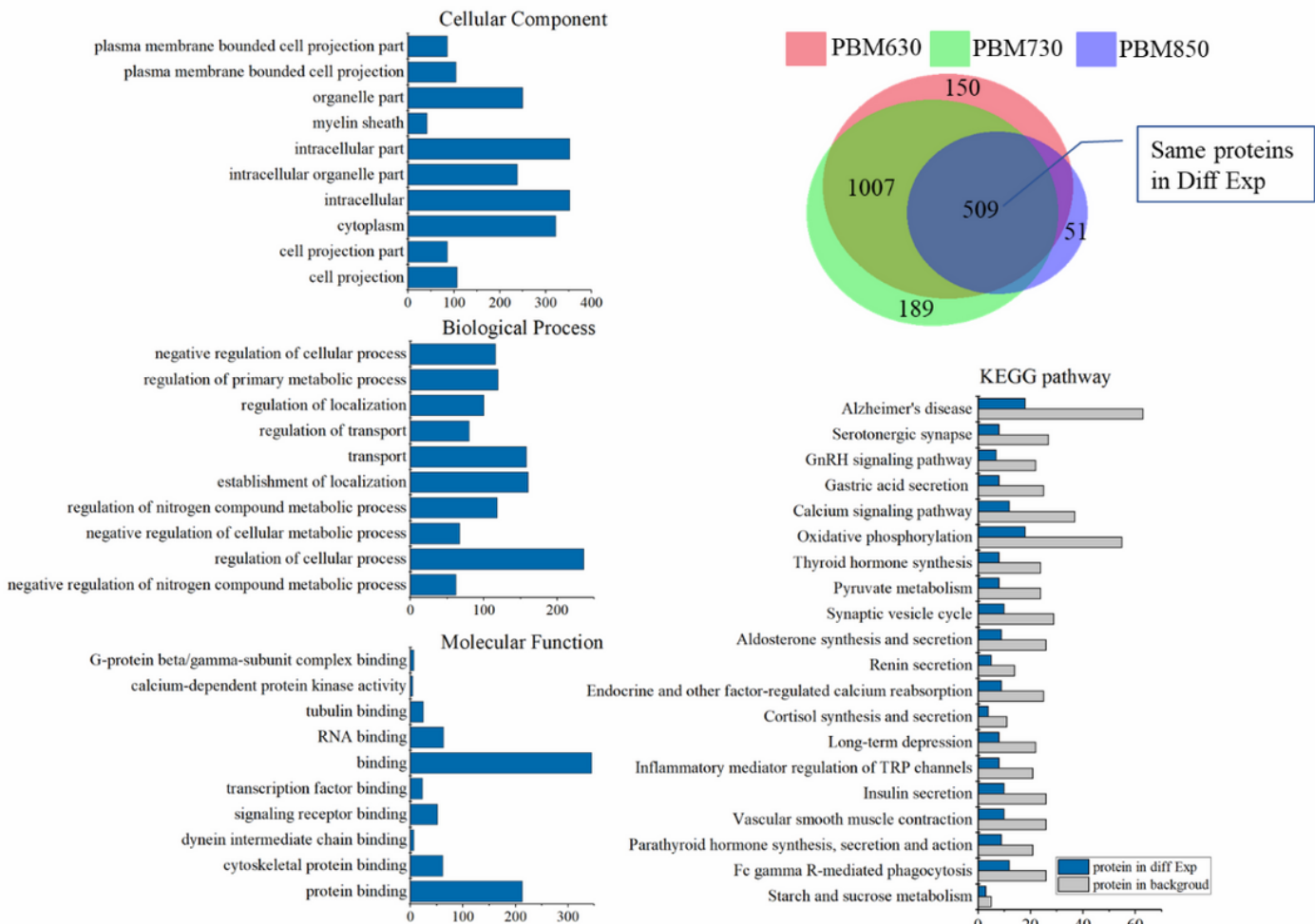


**Figure 7**

GO and KEGG pathway analyses on the common differentially expressed proteins (DEP) among PBM630, PBM730, and PBM850. The Wayne diagram in the upper right corner shows the overlap of DEPs in the three PBM groups. The GO analysis plots show the first ten proteins with the lowest p values, and the KEGG pathway analysis plot shows 20 pathways with  $p < 0.05$ .

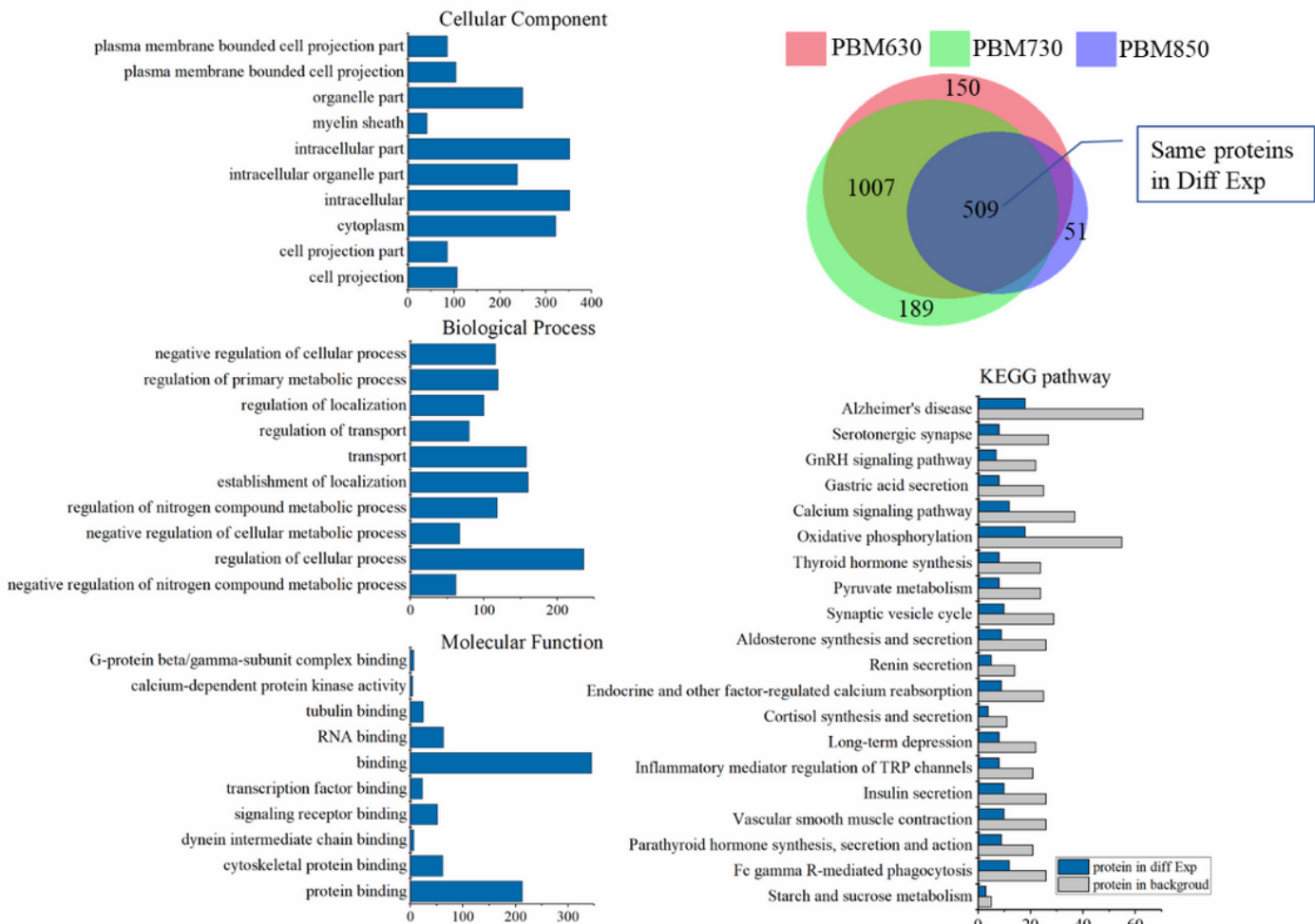


**Figure 7**

GO and KEGG pathway analyses on the common differentially expressed proteins (DEP) among PBM630, PBM730, and PBM850. The Venn diagram in the upper right corner shows the overlap of DEPs in the three PBM groups. The GO analysis plots show the first ten proteins with the lowest p values, and the KEGG pathway analysis plot shows 20 pathways with  $p < 0.05$ .

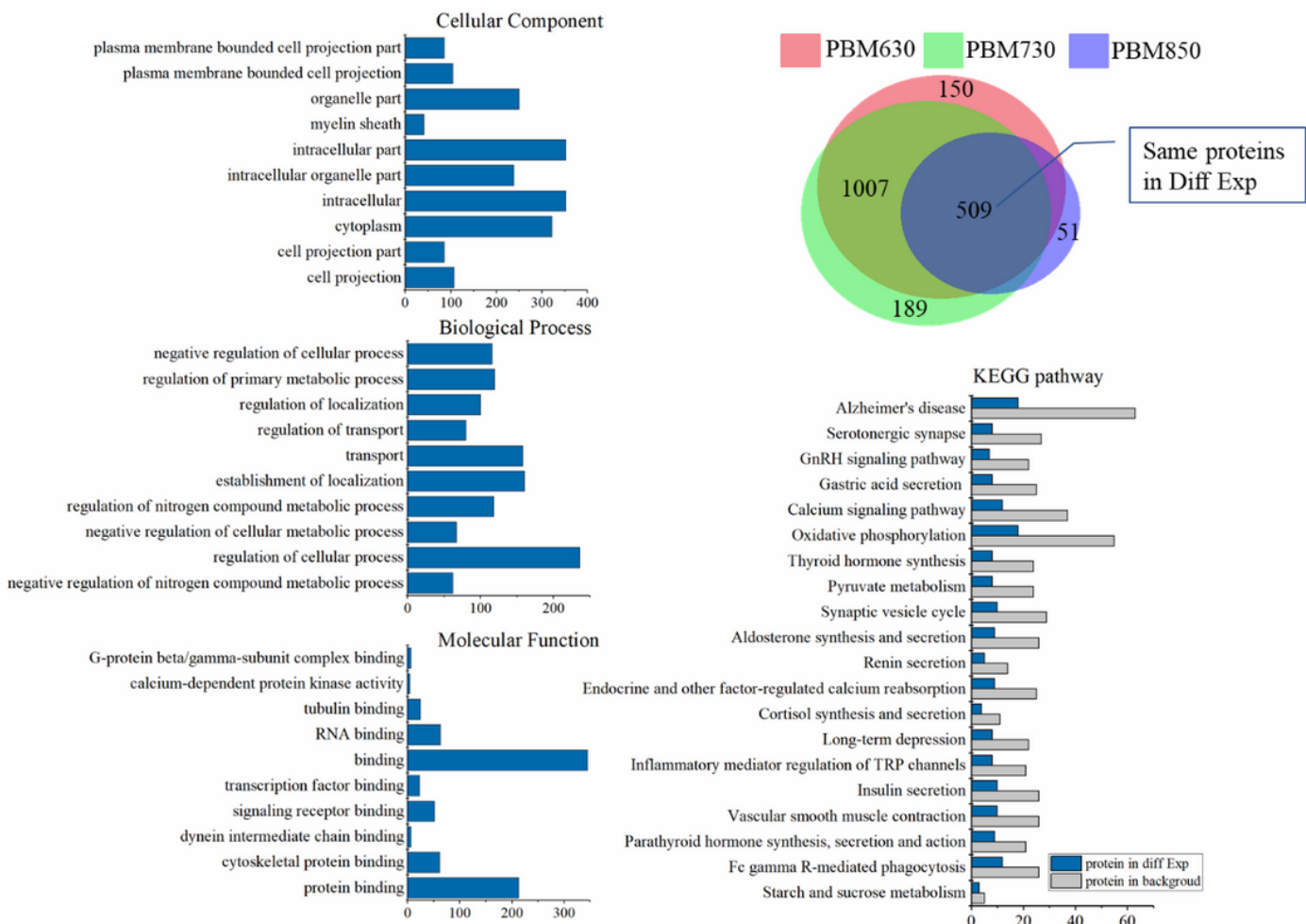


**Figure 7**

GO and KEGG pathway analyses on the common differentially expressed proteins (DEP) among PBM630, PBM730, and PBM850. The Venn diagram in the upper right corner shows the overlap of DEPs in the three PBM groups. The GO analysis plots show the first ten proteins with the lowest p values, and the KEGG pathway analysis plot shows 20 pathways with  $p < 0.05$ .

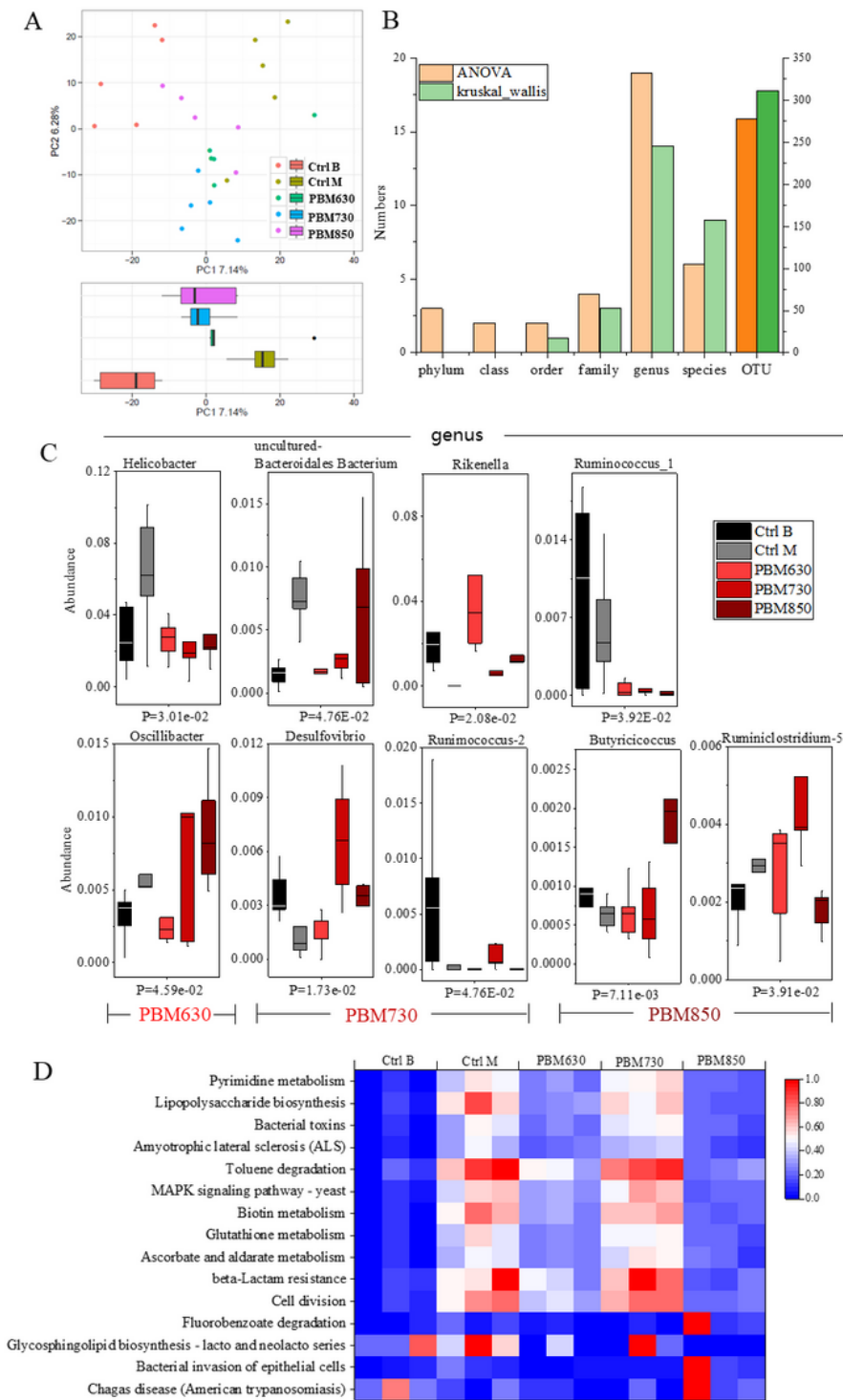


**Figure 8**

Analysis of gut microbiome composition and function prediction in the Alzheimer's disease (AD) mice treated by photobiomodulation (PBM). A. The PCA clusters based on OTU. B. Multivariate statistical analysis of microorganisms. C. Boxplot analyses showing the relative abundance of genus-level bacteria treated by PBM. The first row showed similar improvement effects of PBM630 to PBM850, and the

second row showed the unique effects of the three PBM groups. D. KEGG function prediction based on 16S sequencing data of the groups.

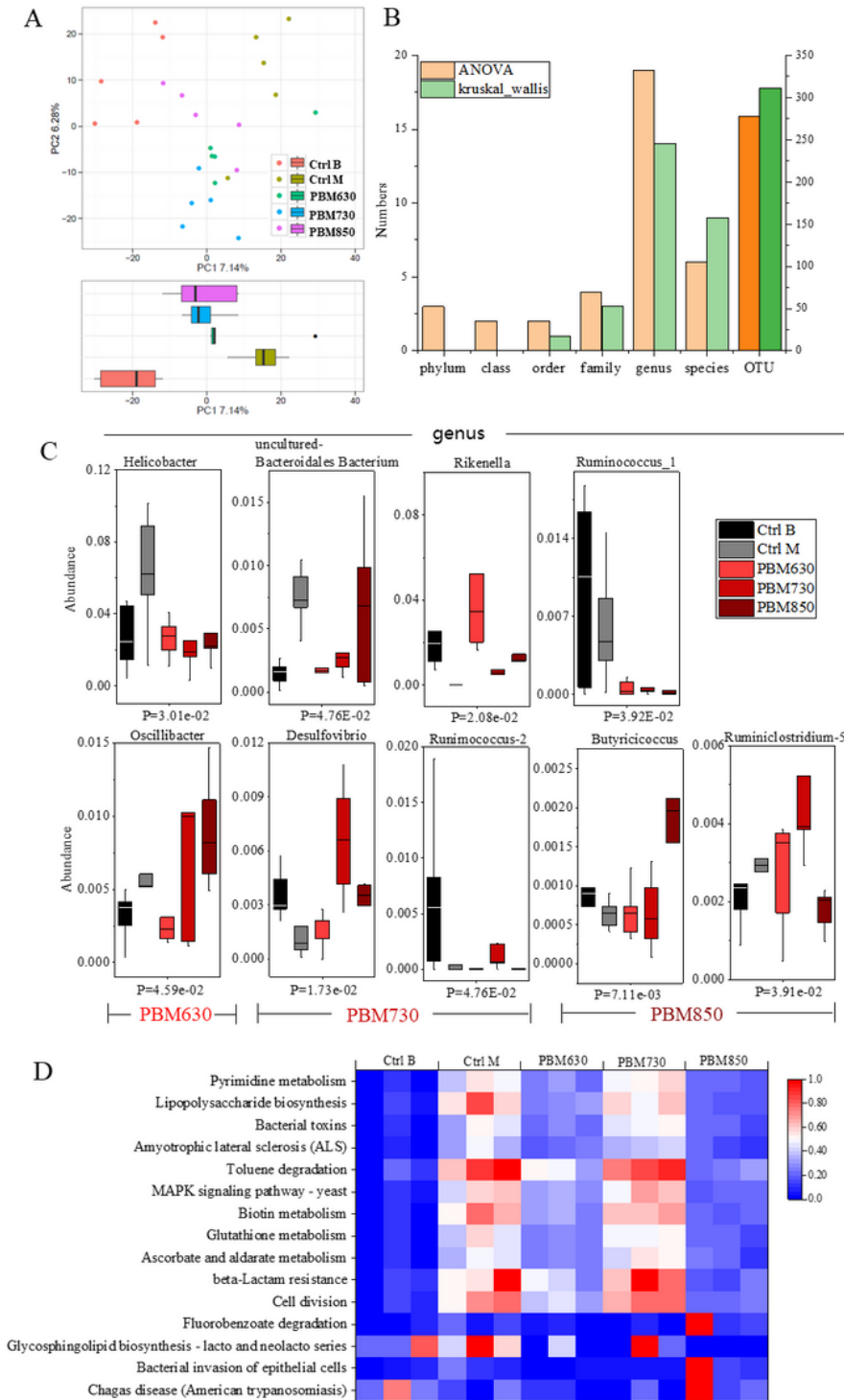


**Figure 8**

Analysis of gut microbiome composition and function prediction in the Alzheimer's disease (AD) mice treated by photobiomodulation (PBM). A. The PCA clusters based on OTU. B. Multivariate statistical analysis of microorganisms. C. Boxplot analyses showing the relative abundance of genus-level bacteria

treated by PBM. The first row showed similar improvement effects of PBM630 to PBM850, and the second row showed the unique effects of the three PBM groups. D. KEGG function prediction based on 16S sequencing data of the groups.

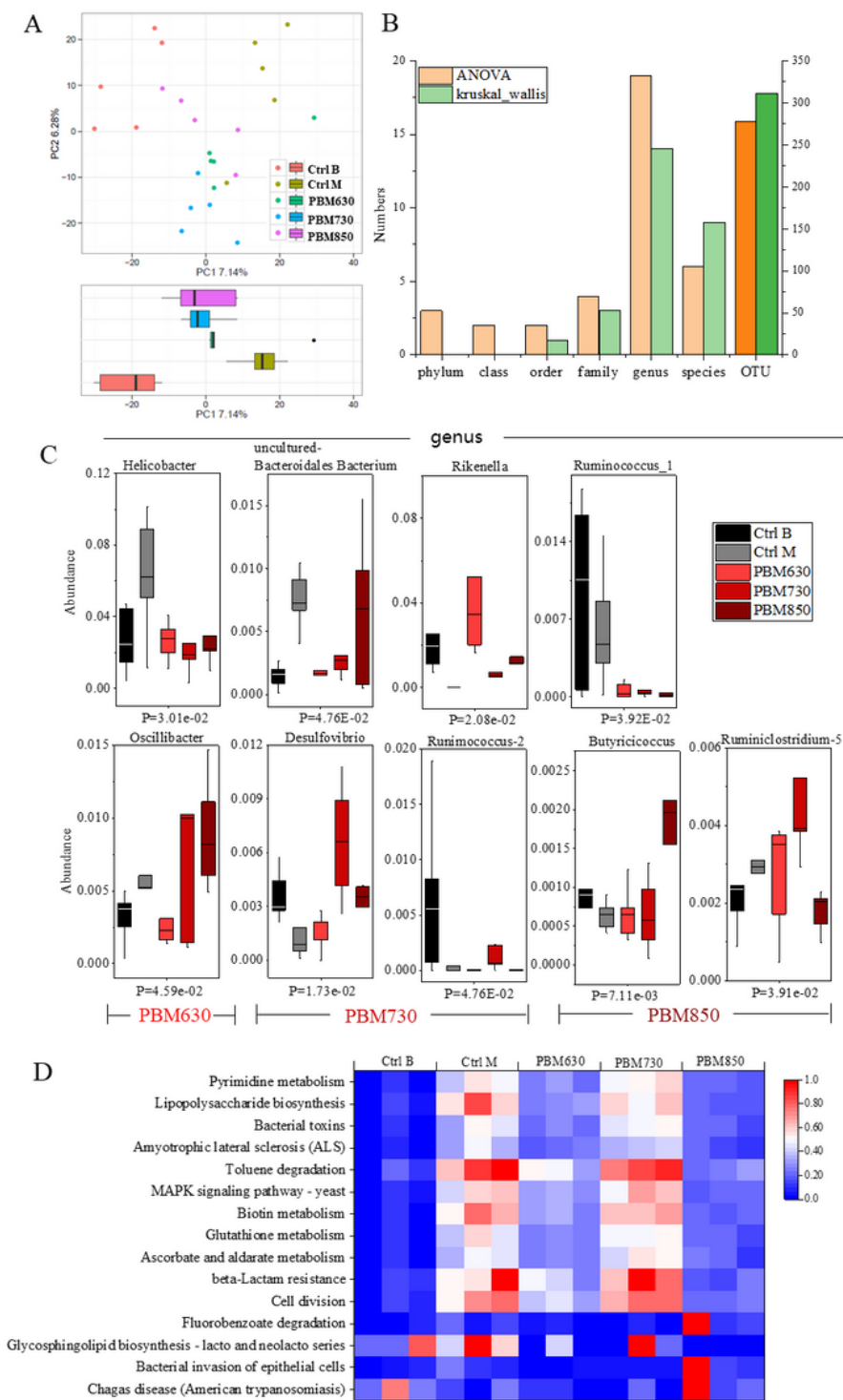


**Figure 8**

Analysis of gut microbiome composition and function prediction in the Alzheimer's disease (AD) mice treated by photobiomodulation (PBM). A. The PCA clusters based on OTU. B. Multivariate statistical

analysis of microorganisms. C. Boxplot analyses showing the relative abundance of genus-level bacteria treated by PBM. The first row showed similar improvement effects of PBM630 to PBM850, and the second row showed the unique effects of the three PBM groups. D. KEGG function prediction based on 16S sequencing data of the groups.